AN ABSTRACT OF THE THESIS OF

Mathieu Georges Charles Martin for the degree of Master of Science in Mechanical Engineering presented on January 27, 2009.

Title: Numerical Study of Flow Maldistribution in Microchannels using Fully Resolved Simulation

Abstract approved: _____

Sourabh V. Apte

This thesis addresses numerical simulation of flow maldistribution in microchannels. Microchannels are often associated with two phase-flows which can generate many problems such as plugging the channel or perturbing the flow. In this study we have used CFD and fully resolved technique to simulate what would happen in the case of bubbles modifying the flow in a 3 parallel microchannels structure. Such perturbations in the domain have a significant impact on the flow rate and on the flow distribution inside the geometry which can cause many disorders in terms of heat exchange for example, where a continuous mass flow rate is essential to be efficient.

To restore a nominal flow, valves are added to the geometry at the entrance of each microchannel. These valves act separately and are operated by a controller to regulate and eventually modify the flow to flush the bubbles out. The

controller makes its decision based on the mass flow rate data provided by sensors located at the entrance and exit of each channel. Based on this information the controller tries to equalize the mass flow rate in each channel. In the case of plugged channel, this means that most of the flow will be forced through the plugged channel to push the bubble out. These valves have an impact on the flow distribution inside the channel but allow an active and accurate control over the flow in the geometry.

In this work the scheme used to solve the two-phase flow problem is crucial. Since the simulation is dealing with both freely (bubbles) and forced (valves) moving particles over the geometry, the formulation has to be able to handle this phenomenon as well as the flow itself in a reasonable amount of time. A fictitious domain technique, allowing high density ratio between fluid and particle, has been used. This new approach has been extensively tested and significantly improved for this application.

Numerical Study of Flow Maldistribution in Microchannels using Fully Resolved Simulation

by

Mathieu Georges Charles Martin

A THESIS

submitted to

Oregon State University

in partial fulfillment of
the requirements for the
degree of

Master of Science

Presented January 27, 2009
Commencement June 2009

Master of Science thesis of Mathieu Georges Charles Martin presented on January 27, 2009.

APPROVED:

Major Professor, representing Mechanical Engineering

Head of the School of Mechanical, Industrial and Manufacturing Engineering

---

Dean of the Graduate School

I understand that my thesis will become part of the permanent collection of Oregon State University libraries. My signature below authorizes release of my thesis to any reader upon request.

Mathieu Georges Charles Martin, Author

ACKNOWLEDGEMENTS

I would like to thank my advisor Dr. Sourabh Apte for his support and his advice. His advice helped me evolve in the field, both from a knowledge point of view as well as maturity about how to approach and understand problems.
Thank you to the students of our CFD group : Ehsan Shams, Stephen Snider, Justin Finn and more recently Andrew Cihonski. I had the opportunity to work with great value people. They provided help and advice, made me think in directions I wouldn't have found on my own and they maintained a great and efficient working atmosphere in the group.
I would like to thank Chris Patton and Dr. John Schmitt who worked on the project with me and developed the controller that is used in my simulations. Their collaboration and contribution to this work have been most beneficial and helped us evolve and develop new approaches.
I also would like to acknowledge the US Army's Tactical Energy systems through Oregon Nano & Micro Institute (ONAMI) who partially funded this study.
I would also like to thank all the TFS professors I have had the chance to meet through my classes. They always provided me with support and helped me, mainly at the beginning when it was not easy to be an international student. I especially want to thank Dr James Liburdy who helped me with paperwork, administrative issues and provided me advice.

I would like to thank my former french graduate school (ISTIL) and the professors who encouraged me to come at Oregon State and who first picked my interest in fluid mechanics : professors Faouzi Laadhari and Jean Bataille.
I would like to thank my parents who supported me to come to the the United States even if it wasn't easy for them. Also I would like to mention my friend (and roommate) Donald Heer who welcomed me when I got here and always supported me, helping me to go through many things. Finally my girlfriend Ellen deserves some credits, she had to cope with my schedule and my late nights of work.

TABLE OF CONTENTS

TABLE OF CONTENTS (Continued)

LIST OF FIGURES

LIST OF FIGURES (Continued)

LIST OF FIGURES (Continued)

LIST OF TABLES

DEDICATION

To my family and the people who care about me.

Chapter 1 – Introduction

Microchannels are present in many applications. They can be used as heat exchangers either to take heat away from a heat source or to carry a heated fluid that needs to be cooled through theses channels. Other applications in chemistry involve micro-mixing or transport of particles. In most of the applications, microchannels are associated with two phase-flows. In the case of heat exchangers, bubbles can appear in the fluid and be transported along the microchannel. These bubbles can cluster together along the walls and form compact structures that can partially or totally plug the channel as shown by Sharp et al. [1]. Such structures happen when the concentration of bubbles increases, and the probability of bubble aggregation increases. The nucleation of the bubbles can also be mentioned. A bubble can grow along the wall, because of a local peak of temperature at the wall of the channel. This bubble remains attached as long as the flow is not strong enough to detach it from the wall. Several forces act to keep the bubble attached to the wall. The main one being the surface tension of the bubble. This case is the one we are trying to reproduce in this study.

Another aspect can be particles flowing with the fluid as in the case of chemical reactions. Microchannel arrays can be used as mixing apparatus to enhance the reaction rate. If one of the products of the reaction is a solid (like a precipitation reaction) then small particles will flow in the channels along with the fluid. Again

following the volume fraction of these particles, the probability of aggregation is more or less high, but they can always cluster along the walls which would perturb the flow in the channel and eventually affect the reaction rate in the other channels by increasing the mass flow rate inside those channels. In this case microchannels can be very fragile and high pressures inside one of the channels could damage the structure of the array. If a sufficient amount of particles cluster along a wall, it could eventually plug the channel and, in some cases, damage the structure.

In this work, direct numerical simulation (DNS) is used in order to resolve two-phase flow in parallel microchannels. DNS is used because of the low Reynolds number involved and the laminar behavior of the flow inside the microchannels. In order to simulate the bubbles in our geometry, a fully resolved technique is used, in which the motion of fluid and particles [1] is obtained from principles, without having to regenerate the mesh every time-step. The algorithm and the numerical scheme used will be described later. Also several test cases will be presented in order to validate this approach along with comparisons of available results from the literature, which will be used to validate the accuracy of our method.

[1] Henceforth a particle may represent a dispersed phase in the form of solid particles or vapor/gas bubbles.

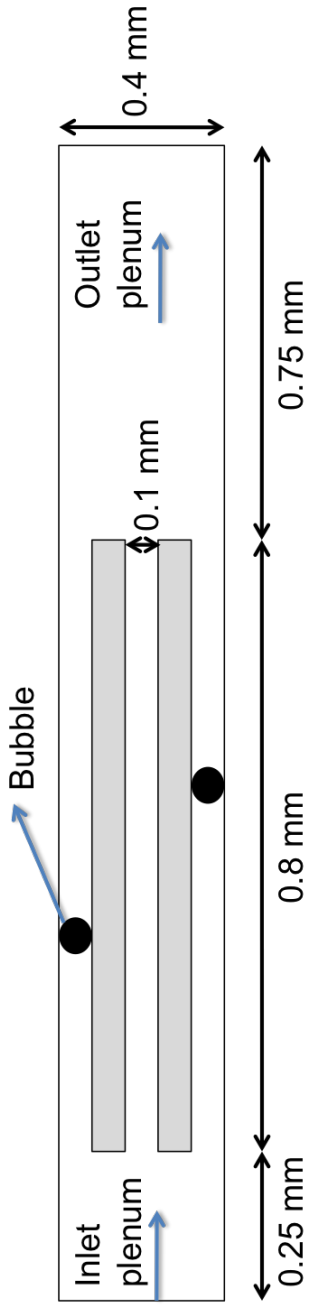

Figure 1.1: Schematic of parallel microchannels with bubbly flow and flow maldistribution.

Using the previously mentioned approach this work presents simulations of spherical rigid bubbles flowing in a 3 parallel microchannels structure. Figure 1.1 presents the geometry that is going to be used; it also shows an illustration of flow maldistribution in the 3 parallel microchannels geometry. The effect of a bubble partially plugging a channel will be investigated. As mentioned earlier the bubble plugging the channel doesn't only have an effect on the flow inside its channel, but it also significantly modifies the flow inside the connected channels. In order to provide a solution to that problem and to actively help restore a nominal flow inside the entire structure, valves are used at the entrance of each channel to regulate the flow. These valves are independent and operated by a controller. The goal of these valves is to equalize the flow rate inside each channel, which helps to restore the flow if a bubble, or an obstruction is detected. A detailed description of the behavior of the valves and their effect on the flow will be presented.

The goal of this work is to show our ability to provide a dynamic solution to a fairly common problem with two-phase flows in microchannels. The results shown in this thesis are based only on numerical simulations. Even if it is unlikely to see the apparatus simulated here, the present work shows that it is possible to have an active control on the mass flow rate of microchannel structure and that a controller can be designed in order to achieve an optimal flow through this channel with the ability to react in the case of an obstruction.

In a the next chapter, a brief overview over the main aspects in this study will be presented through relevant references from the literature. Then the next section will present the numerical formulation and the research flow solver used

to solve the flow, before, in the following section, to validate it with elementary cases necessary to ensure the accuracy of the solver. Finally, the simulations of the two-phase flow through the three-channel geometry will be presented.

The work presented in this thesis has been published in a the Journal of fluids Engineering [2] and will be presented at the 3rd International Conference on Micro- and Nanosystems (MNS) (ASME conference in San Diego in August 2009) [3].

Chapter 2 – Literature review

This chapter presents an overview of the current state of the knowledge about the different issues tackled in this work. Three different aspects necessary to the global understanding of this work are described in the following paragraphs. Since we are dealing with bubbles in microchannels, a brief introduction on two-phase flow regimes is presented. Then the bubble nucleation process and dynamics associated with the bubble growth is presented and finally some cases of controlled flows are shown.

Microchannels are used in many applications. The literature presents many cases involving heat exchange. A fluid flowing in the microchannels is used to take heat away and cool down certain devices. If the temperature becomes too high in one of the microchannels, a bubble can be created. This bubble can have several different behaviors following the fluid parameters, the flow, the temperature, and the roughness of the wall. The next section presents the different regimes that can occur in bubble formation.

2.1 Two-phase flow regimes

Two-phase flows in micro-channels have been widely explored. Several studies show the different patterns of a multiphase flow in micro-channels [4, 5].

The vapor phase can take several forms inside the channel which causes different behaviors in the flow. Cubaud et al. [6] present the different regimes of two-phase flow in a square channel. These regimes are determined by the size and the occupation of the channel by the vapor phase. The first regime is the bubbly flow where relative small bubbles compared to the size of the channel flow with the fluid. For this regime the bubbles are mainly spherical and once they detatch from the wall, their velocity is close to the flow velocity due to low Stokes number. Clogging or arching structures can occur inside the channel or in sharp corners due to the interaction of the bubbles between each other [7]. Our simulation is based on this regime (see figure 1.1).

The other regimes concern longer bubbles where the length of the bubble is larger than the channel height. In the wedge flow regime, the velocity of the vapor phase becomes slower and the layer of fluid is thinner between the vapor and the wall. If the bubble keeps growing it turns to a slug flow and the liquid fraction lowers $\alpha_L < 0.2$. If the bubble becomes long enough so that its size becomes the same as the channel length, then the liquid flows around the bubble. This leads to the annular flow [8]. Finally the last regime, dry flow, occurs when the void fraction $\alpha_g > 0.995$. The vapor phase is no longer moving and no liquid flows along the walls of the channel. All the flow happens in the wedges.

2.2 Bubble nucleation

Wang et al [9] show experimental results and visualization of bubble nucleation. They have looked at transitional flow variations during the bubble growth along the wall of a microchannel using PIV. The flow applied through the channel is slow ($Re = 0.02$) to maintain a Stokes regime so that the force applied on the bubble by the flow is not large enough to detach the bubble from the wall. They have found that the total drag force of the bubble is very small compare to other forces such as surface tension. In this particular case they have been able to write a balanced equation for a static bubble involving all the acting forces. A pressure has been determined in order to balance the static equation. This pressure corresponds to the pressure drop required to balance the forces around the bubble. If, because of an increase in the mass flow rate, the pressure drop increases then the hydrodynamic force will be large enough, to overcome the other forces and then the bubble will be released. A departure criterion can be defined from the pressure used, to balance the equation for a static bubble.

Lee et al. [10] (in the case of a single channel) and Li et al. [11] (in the case of two parallel microchannels) have studied the bubble dynamics. These studies look at the bubble behavior in one or two microchannels. The bubble nucleation speed, growth, and frequency have been observed. Also a departure criterion function of the size of the bubble has been proposed. This criterion is a function of the pressure drop around the bubble. As mention in the previous paragraph the departure of the bubble happens when the liquid force becomes sufficient to overcome the forces

that keep the bubble attached to the wall. Here the departure criterion is a function of the size of the bubble. Indeed, surface tension is stronger for smaller radii. But, at the same time the force of the flow is fairly small since the area of the bubble to the flow is not very big. With its growth, the force applied on the bubble increases and the surface tension becomes weaker. Therefore a departure criterion can be defined based on the size of the bubble. The same behavior is observed in both situations (single and two channels). However, in the case of two parallel channels a limitation exists in the force that the flow can apply since it will have a tendency to follow the easier path (unpluged channel). Therefore the departure will be a function of the mass flow rate whereas in the single channel case the entire flow is forced to go through the same channel.

2.3 Flow control

Active flow controls has already been used in the literature for the same type of geometry involving microchannels. Bleris et al. [12] have used that technique in order to improve mixing of chemical species into a reactor. The geometry is composed of three inlets on the left side and two outlets on the right side. Through the middle inlet, chemicals are introduced. The goal of the controller is then to control the concentration of the chemicals in the two outlets by modifying only the flow in the top and bottom outlet. By acting on the mass flow rate through the top and bottom inlet, the controller can enhance the mixing in the central plenum between the chemicals and the fluid. It can also locate these chemicals on

one side or another following the concentration of chemical wanted through one outlet or another. The MPC controller gives very good results once the steady state is achieved and the chemicals can be directed very accurately through the outlet (uniformly, or entirely through one outlet).

Mukherjee et al. [13] presents a numerical study of bubble growth inside microchannels. Bubble nucleation and rapid growth in microchannels with a common head can strongly perturb the flow and even lead to reverse flows. The liquid tends to flow through the least plugged channel. It has been shown that the upstream interface of the bubble can move towards the inlet of a channel. This phenomenon can lead to reverse flows in the microchannel. In order to address this problem, Mukherjee et al. proposes the use of variable cross section shapes in order to force the flow towards the outlet. If the cross-section at the inlet is smaller then the pressure will be higher at that point which will prevent reverse flows from going through this section of the channel. This case is very close to the work presented in this thesis, however they use a passive method to regulate the flow whereas in the work presented here an active control is used which allows better flexibility and efficiency in terms of effects on the global flow through the geometry.

Other two-phase flow applications can be seen in particle transport. Using the density of different materials, particles are directed in one or the other direction by buoyancy or electromagnetic forces. Small flowing particles can cluster and interact with the walls in order to create structures which may partially block one channel [1].

Chapter 3 – Research flow solver and numerical methods

To handle two-phase flows one must be able to solve the flow in a domain and also particles motion, along with their interactions with the flows. Several techniques can be used to solve such flows: point particle approach (Euler-Lagrange), fully resolved simulation (used in this study) and two-fluid model (Euler-Euler) [14]. In the point-particle approach the interaction forces between fluid and particles can be computed by modeling the drag and lift forces on the particles using an empirical model. This type of technique allows to solve two-phase flows involving a large number of particles with a fairly coarse grid since the shape of the particles is not actually resolved, only the interaction forces are simulated.

The work presented in this thesis uses a fully-resolved technique. This technique requires the grid to be fine enough in order to properly resolve the shape of the particles. The shape of the particles is actually added to the geometry and the momentum equations are solved in the domain considering the presence of the particles. This chapter presents the algorithm and the main numerical steps used to solve the flow and the particles motion.

3.1 Mathematical formulation

One of the keys of this work is the the ability to solve the flow while dealing with moving valves and bubbles. Direct numerical simulation has been used to solve the flow. The goal of this simulation is to be able to solve a flow with moving particles (bubbles or valves) inside the domain without having to regenerate the grid at each time step. To do this, a fictitious domain technique has been used. This technique allows to generate a uniform cartesian grid over all the geometry and defines the valves and bubbles on top of this mesh numerically which therefore eliminates the need to modify the grid. A detailed description of the numerical approach can be found in Apte et al. [15].

This type of technique has been described in the literature (Glowinski et al. [16], Patankar [17], Apte et al. [15]). Also in order to improve the speed of the simulation the flow solver is fully parallel using Message Passing Interface. As mentioned earlier what made this simulation possible is the ability to simulate moving bodies inside the flow without re-generating the grid.

Let's consider a computational domain Γ. This domain contains fluid and particles. $\Gamma_F(t)$ represents the part of the domain occupied by the fluid and $\Gamma_P(t)$ represents the domain occupied by the particles. For the purpose of this description only one particle is assumed to be inside the domain. The main idea of the fictitious-domain approach as developed in Glowinski et al. [16] is to assume and to solve for fluid over all the domain Γ, even over $\Gamma_P(t)$. Only the properties of the fluid change inside the particles, such as density (ρ_P) or viscosity (μ_P). The fluid is

assumed to be incompressible over the domain. The particles are also assumed to be rigid, thus a rigidity constraint will be applied to the particles so that they can be treated as rigid bodies. We'll see later how this rigidity constraint is obtained. For simplicity Dirichlet boundary conditions are assumed at the boundaries of Γ.

Equation 3.1 shows the general momentum equation over the entire domain. Equation 3.2 is the continuity equation.

$$\rho\left(\frac{\partial \mathbf{u}}{\partial t} + (\mathbf{u}\cdot\nabla)\,\mathbf{u}\right) = -\nabla p + \nabla\left(\mu_f\left(\nabla\mathbf{u} + (\nabla\mathbf{u})^T\right)\right) + \rho\mathbf{g} + \mathbf{f} \quad (3.1)$$

$$\frac{\partial \rho}{\partial t} + \nabla\cdot(\rho\mathbf{u}) = 0 \quad (3.2)$$

where ρ is the density over the entire domain and is defined by equation 3.3, μ_F is the kinematic viscosity of the fluid, $\mathbf{g}$ is the acceleration of gravity and $\mathbf{f}$ is the body force used to enforce the rigidity constraint inside the region Γ_P.

$$\rho = \rho_f\,(1-\Theta_p) + \rho_p\Theta_P \quad (3.3)$$

$$\Theta_P = \begin{matrix} 0 & \text{in } \Gamma_F \\ 1 & \text{in } \Gamma_P \end{matrix} \quad (3.4)$$

where ρ_F is the density of the fluid and ρ_P is the density in the particle region. Θ_P is a function defined by equation 3.4. This function is used to locate the the particle over the domain. It takes the value of 1 inside the particle and 0 outside, however the transition is not sharp between the particle and the fluid, and, following the refinement of the grid, the interface between fluid and particle can be more or less thin, therefore the transition between 0 and 1 is more or less sharp and Θ takes

values between 0 and 1 in a thin region around the interface.

The Navier-Stokes equations can be simplified with the incompressibility assumption. This assumption is valid for the flow in the cases studied because of the conditions and the low velocity of the flows. It also remains valid inside the particle region Γ_P since a rigidity constraint is applied ensuring that the volume of the particle won't change. This assumption leads to equation 3.5 and 3.6.

$$\rho\left(\frac{\partial \mathbf{u}}{\partial t} + (\mathbf{u}\cdot\nabla)\,\mathbf{u}\right) = -\nabla p + \mu_f\left(\nabla^2\mathbf{u}\right) + \rho\mathbf{g} + \mathbf{f} \tag{3.5}$$

$$\nabla\cdot\mathbf{u} = 0 \tag{3.6}$$

In the following part, the main steps of the algorithm that solves flow and particles is shown.

1. The first step consists in solving the momentum equation 3.5 over all the domain Γ without any distinction between fluid and particles. ρ is set to ρ_F and the extra force term $\mathbf{f}$ is set to 0. Equation 3.5 is then solved using a classic fractional-step scheme. The continuity in the domain is enforced by solving a Poisson equation for the pressure.

   The solution of equation 3.5 is a velocity field $\widetilde{u}$. This velocity field is the actual solution of the flow outside the objects $(\Gamma_F) : \widetilde{u} = u^{n+1}$. The velocity to the region of the particle Γ_P needs to be calculated. This is done by adding a body force $\mathbf{f}$ to the momentum equation as shown in equation 3.5. This is motivated by the fact that the object needs to move as a rigid body, therefore this extra term needs to be applied in the region where the particle

is located. The density as well needs to be defined in function of the location of the objects in the domain. The density ρ inside the domain is defined by equation 3.3 where $\Theta_P = 0$ over Γ_F and $\Theta_f = 1$ over Γ_P.

2. Now that we have the solution for the flow we need to get the solution over Γ_P. To do this we apply the rigidity constraint in the particle domain and solve for $\mathbf{u}^{n+1}$ based on the velocity field $\widetilde{\mathbf{u}}$ (equation 3.7).

$$f = \rho_P \frac{(\mathbf{u}^{n+1} - \widetilde{\mathbf{u}})}{\Delta t} \tag{3.7}$$

where Δt is the time step.

To be able to solve for $\mathbf{u}^{n+1}$ we need to get an expression for the force term $\mathbf{f}$, this is where the rigidity constraint is applied. This rigidity constraint is defined by the rigidity assumption and hence there shouldn't be any deformation inside the object. Several ways of obtaining the rigidity constraint have been proposed ([16, 18, 17]). We follow the formulation developed by Patankar [17] and described in detail by Apte et al. [15]. A brief description is given here for completeness. The rigidity of an object can be expressed by forcing the deformation-rate tensor $D[u]$ (equation 3.8) to be 0 and therefore the velocity computed from the momentum equation including the body force term is the velocity of the rigid body. This velocity (equation 3.13) has to be applied in the region occupied by the body.

$$D[\mathbf{u}] = 0.5\left(\nabla\mathbf{u} + \nabla\mathbf{u}^T\right) = 0 \tag{3.8}$$

From equations 3.7 and 3.8 we obtain the gradient of the deformation-rate tensor for $\mathbf{u}^{n+1}$:

$$\nabla \cdot \left(D\left[\mathbf{u}^{n+1}\right]\right) = \nabla \cdot \left(D\left[\widetilde{\mathbf{u}} + \frac{\mathbf{f}\Delta t}{\rho}\right]\right) = 0 \tag{3.9}$$

$$D\left[\mathbf{u}^{n+1}\right] \cdot \mathbf{n} = D\left[\widetilde{\mathbf{u}} + \frac{\mathbf{f}\Delta t}{\rho}\right] \cdot \mathbf{n} = 0 \tag{3.10}$$

The velocity of the rigid body $\mathbf{u}^{RBM}$ is decomposed into its translational (equation 3.11) and rotational (equation 3.12) components. The velocity of the rigid body can then be easily computed with equation 3.13.

$$M_p\mathbf{U} = \int_{\Gamma_P} \rho\widetilde{\mathbf{u}} dV \tag{3.11}$$

$$I_p\mathbf{\Omega} = \int_{\Gamma_P} \rho\widetilde{\mathbf{u}} dV \tag{3.12}$$

$$\mathbf{u}^{RBM} = \mathbf{U} + \Omega \times \mathbf{r} \tag{3.13}$$

where M_p is the mass of the body, I_p is the moment of inertia and $\mathbf{r}$ is the position vector of a point in the object from the centroid of the object.

Therefore the velocity of the particle is defined and can be applied in the region of the object ($\mathbf{u}^{n+1} = \mathbf{u}^{RBM}$). It is now possible to find $\mathbf{f}$ with equation 3.7 which leads to equation 3.14.

$$f = \rho_P \frac{\left(\mathbf{u}^{RBM} - \widetilde{\mathbf{u}}\right)}{\Delta t} \tag{3.14}$$

3. The rigidity constraint can now be applied to the force term $\mathbf{f}$ in a third

fractional step using equation 3.7.

In the approach detailed above the entire domain is considered and solved as a fluid. An extra term is added to enforce the rigidity of the particles in the region of the particle only. An uncertainty persists at the boundary of the particle since the transition between the 2 regions Γ_P and Γ_F is not sharp. The force term representing the rigidity constraint will then be smeared between 0 and its value. This, might cause some errors, however in the validation cases we have run, the cases which requires good resolution of the boundary gives very good agreement with experimental results (cylinder, sphere cases).

3.2 Numerical formulation

In this approach, one of the key element is to locate and define the particles in the fluid domain. The particles are represented by material volumes. Typically these material volumes are cubic and have the same properties as the object (density, viscosity, velocity). Because of the rigid-body assumption, no relative velocity is allowed among the material volumes.

To create the object, a cubic cartesian sub-grid is generated inside a bounding box and then the shape is computed from a centroid. The distance of each material volume is computed from the centroid of the object which allows us to eliminate the material volumes that do not lay inside the final shape. From this approach it is obvious that shapes are being represented with small cubic volumes, this is why a fairly good resolution is important in order to achieve a good resolution of the

final shape, especially if the shape is circular.

Properties of the object (density, volume fraction) contained in the material volumes are interpolated onto the background mesh. A kernel type interpolation is used in order to interpolate the properties onto the background grid. In order to optimize the interpolation both the background mesh and the material volumes resolution needs to be appropriate to achieve a good resolution of the shape.

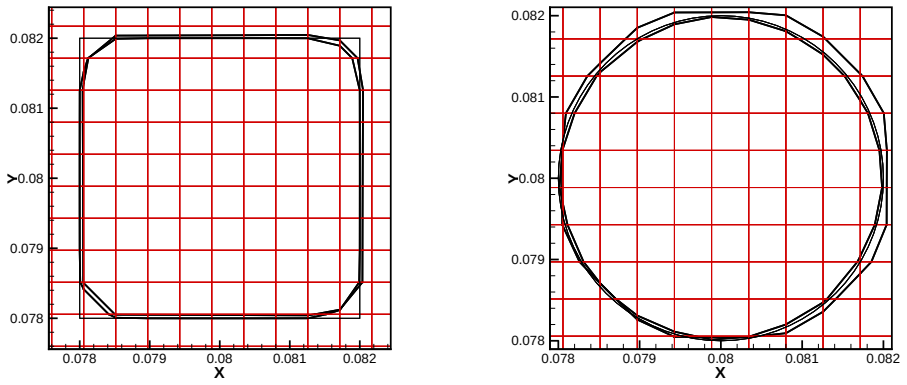

(a) (b)

Figure 3.1: Comparison of elementary geometry reproduced by cubic material volumes. The figures show a comparison between the real geometry (thin line), the representation using 1 material volume per grid cell and the representation using 4 material volumes per grid cell. Plotted is the volume fraction of 0.5 for each resolution of material volume. Figure 3.1a shows the representation of a square. Figure 3.1b shows the representation of a circle.

Figures 3.1 show the representation of an elementary geometry for several resolutions of the material volumes over the background mesh. The increase of the number of material volumes help resolve the real shape of the geometry. In the case of the circle (figure 3.1b) using 4 material volumes per grid cell allows to represent

the shape of the circle exactly. However in the case of the square (figure 3.1a) the increase in the resolution of material volumes does not significantly improve the resolution of the shape. This is due to the coarse grid used as the background mesh that cannot properly capture the geometry even with a sufficient number of material volumes.

As mentioned earlier the velocity of the rigid body is defined as $\mathbf{u}^{RBM} = \mathbf{U} + \mathbf{\Omega} \times \mathbf{r}$ where $\mathbf{U}$ is the translational velocity, $\mathbf{\Omega}$ is the angular velocity and $\mathbf{r}$ the position relative to the centroid of the body. Based on the velocity field calculated earlier the translational velocity of the material volume has to be the same for all the material volumes and the centroid. However due to the angular velocity the position of the material volumes need to be updated with respect to the centroid of the rigid body.

In order to handle multiple particles collisions a model based on the one described in Glowinski et al. [16] is implemented. The position of each particle is computed and compared to all the other particles in order to avoid overlapping between them. In case of contact, a repulsive force is added to the particles colliding in order to model the collision. The case of collision with a wall is handled in the same way by assuming a mirror particle symmetric with respect to the wall, then the collision is handled as described before.

3.3 Discretization and numerical algorithm

The mathematic formulation of the codes that allows the simulation of rigid immersed bodies has been covered earlier since the fictitious domain approach is a key feature of the work presented in this thesis. The previously mentioned approach sets up the equations for the behavior of the flow and particles over the domain. In order to solve this flow, specific numerical algorithms are used. If a detailed explanation of the numerical schemes involved is not in the scope of this thesis a brief summary of the main steps is presented.

The Navier-Stokes equations (equations 3.5 and 3.6) are discretized using finite volume approach. These equations are discretized and solved for every single control volume of the domain after integrating them over the control volumes.

Equation 3.15 shows the discretized continuity equation.

$$\frac{\rho_{cv}^{n+3/2} - \rho_{cv}^{n+1/2}}{\Delta t} + \frac{1}{V_{CV}} \sum_{faces\ of\ cv} \rho_{face}^{n+1} u_N^{n+1} A_{face} = 0 \tag{3.15}$$

where the subscript "face" corresponds to the value located at the center of the faces, A_{face} is the area of the face, V_{CV} is the volume of the current control volume. The density field ρ is defined by the volume fraction Θ over the domain (equation 3.16):

$$\rho_{cv} = \rho_F \Theta_F + \rho_P \Theta_P \tag{3.16}$$

where ρ_P and ρ_F, are respectively the density of the particle and the fluid and

given as a parameter.

Equation 3.17 shows the discretized momentum equation.

$$\frac{g_{i,cv}^{n+1} - g_{i,cv}^{n}}{\Delta t} + \frac{1}{V_{CV}} \sum_{faces\ of\ cv} g_{i,face}^{n+1/2} u_N^{n+1/2} A_{face} = -\frac{\partial}{\partial x_i} p_{cv}^{n+1} + \frac{1}{V_{CV}} \sum_{faces\ of\ cv} (\tau_{ij})_{face}^{n+1/2} N_{j,face} A_{face} + f_{i,cv}^{n+1} \tag{3.17}$$

where $g_i = \rho u_i$ is the momentum in the i^{th} direction, $\tau_{i,j}$ is the viscous stress tensor and $N_{j,face}$ corresponds to the normal to the face in the j^{th} direction, f_i corresponds to extra force term added inside particle regions. Values at time $n+1/2$ are obtained using a Crank-Nicholson time averaging.

The solver uses a collocated grid which means that pressure, velocity of the fluid and other transport properties are stored at the center of the control volume (cv). This allows to use structures cartesian as well as unstructured or tetrahedral grid. For simplicity of the implementation and to ensure good conservation properties variables are staggered in time : particle position, density, volume fraction and viscosity are stored at $t^{n+1/2}$ and $t^{n+3/2}$, whereas the particle and fluid velocity, the pressure and the rigid body extra force term are stored at t^n and t^{n+1}. Mass and energy conservation are ensured with the use of such grid arrangements. Figure 3.2 summarizes the variable storage in time and space.

The equations 3.16 and 3.17 are solved using an iterative semi-implicit numerical scheme. In order to fully understand the numerical scheme involved the steps are listed below.

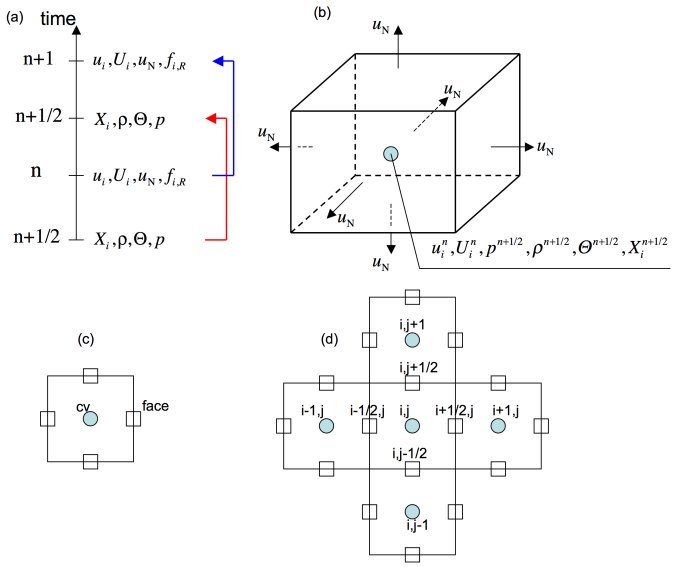

Figure 3.2: Schematic of the variable storage in time and space: (a) time-staggering, (b) three-dimensional variable storage, (c) cv and face notation, (d) index notation for a given k-index in the z direction. The velocity fields (u_i, u_N) are staggered in time with respect to the volume fraction (Θ), density (ρ), and particle position (X_i), the pressure field (p), and the rigid body force ($f_{i,R}$). All variables are collocated in space at the centroid of a control volume except the face-normal velocity u_N which is stored at the centroid of the faces of the control volume.

The algorithm described below corresponds to 1 time-step, however the entire process can be iterated is necessary over the same time-step in order to achieve a correct solution.

1. The first step is to choose predictors, which are a guess of the value of the variables at the next time step. This is achieved by using second order Adams-Bashforth (explicit) for the velocity and backward Euler for the pressure. The rigid-body constraint is updated using interpolation over the material volume and using the predictors of velocity.

$$u_N^{n+1,0} = 2u_N^n - u_N^{n-1} \tag{3.18}$$

$$U_{i,P}^{n+1,0} = 2U_{i,P}^n - U_{i,P}^{n-1} \tag{3.19}$$

$$u_{i,cv}^{n+1,0} = 2u_{i,cv}^n - u_{i,cv}^{n-1} \tag{3.20}$$

$$\Omega_{i,P}^{n+1,0} = 2\Omega_{i,P}^n - \Omega_{i,P}^{n-1} \tag{3.21}$$

2. The particle position is advanced from $t^{n+1/2}$ to t^{n+1} using the predictors defined in the previous step. With the new particle position the volume fraction Θ^{n+1} hence the density field ρ^{n+1} can be calculated.

$$X_{i,M}^{n+1} = X_{i,P}^{n+1/2} + R_{ij}\left(X_{j,M}^{n+1/2} - X_{j,P}^{n+1/2}\right) + U_{i,M}^{n+1,0}\frac{\Delta t}{2} \tag{3.22}$$

3. The momentum equation (equation 3.17) is solved using the fractional step method for the time $n+1$. This is the first step of the fractional step algorithm where the velocity field is solved all over the domain using the old

pressure gradient.

$$\frac{\rho_{cv}^{n+1}\hat{u}_{i,cv}^{k+1} - \rho_{cv}^{n}u_{i,cv}^{n}}{\Delta t} + \frac{1}{V_{cv}}\sum_{faces\ of\ cv}\hat{g}_{i,face}^{k+1/2}u_N^{k+1/2}A_{face} =$$
$$-\frac{\partial}{\partial x_i}\left(p_{cv}^{n+1,k}\right) + \frac{1}{V_{cv}}\sum_{face\ of\ cv}\hat{\tau}_{ij,face}^{k+1/2}N_{j,face}A_{face} + f_{i,cv}^{n+1,k} \tag{3.23}$$

where

$$\begin{aligned}
\hat{g}_{i,face}^{k+1/2} &= \frac{1}{2}\left(g_{i,face}^{n} + \hat{g}_{i,face}^{k+1}\right) \\
\hat{\tau}_{ij,face}^{k+1/2} &= \mu_F\left[\frac{1}{2}\left(\frac{\partial u_i^n}{\partial x_j} + (\frac{\partial \hat{u}_i^{k+1}}{\partial x_j}\right) + \frac{1}{2}\left(\frac{\partial u_j^n}{\partial x_i} + (\frac{\partial \hat{u}_j^{k}}{\partial x_i}\right)\right]_{face} \\
u_N^{k+1/2} &= \frac{1}{2}\left(u_N^n + u_N^{k+1}\right)
\end{aligned}$$

4. The old pressure gradient is removed from the calculated velocity field.

$$\hat{\hat{g}}_{i,cv}^{k+1} = \hat{g}_{i,cv}^{k+1} + \Delta t\frac{\partial}{\partial x_i}\left(p_{cv}^{n+1,k}\right) \tag{3.24}$$

5. The momentum is interpolated between control volumes to get the face-normal velocity.

$$\hat{\hat{g}}_{N}^{k+1} = \frac{1}{2}\left(\hat{\hat{g}}_{i,icv1}^{k+1} + \hat{\hat{g}}_{i,icv2}^{k+1}\right)N_{i,face} \tag{3.25}$$

6. The continuity is enforced by solving for the pressure equation. A new velocity field satisfying continuity is obtained at the face-center. To solve the

pressure Poisson equation, algebraic multigrid is used to speed up the computation. This technique uses a fictitious coarser grid to compute the solution to the Poisson equation. The codes uses BoomerAMG from the library hypre [19].

$$\sum_{faces\ of\ cv} \frac{\delta}{\delta N}\left(p_{cv}^{n+1,k+1}\right) A_{face} = \frac{1}{\Delta t} \sum_{facesofcv} \hat{\hat{g}}_N^{k+1} A_{face} + V_{cv} \frac{\delta \rho_{cv}^{n+1}}{\delta t} \quad (3.26)$$

7. The face-normal velocity is updated with the newly calculated velocity.

$$u_N^{n+1,k+1} = \frac{1}{\rho_{face}^{n+1}} \left(\hat{\hat{g}}_N^{k+1} - \Delta t \frac{\delta}{\delta N} p_{cv}^{n+1,k+1} \right) \quad (3.27)$$

8. The pressure gradient and velocity are reconstructed at the control volume centers based on the pressure calculated at the faces. This step is the last step of fractional step scheme for single phase flow.

$$\frac{\delta p^{n+1,k+1}}{\delta x_i} = \left(\frac{\delta p^{n+\bar{1},k+1}}{\delta N} \right)^{face \rightarrow cv} \quad (3.28)$$

$$u_{i,cv}^{*,k+1} = \frac{1}{\rho_{cv}^{n+1}} \left(\hat{\hat{g}}_{i,cv}^{k+1} - \Delta t \frac{\delta}{\delta x_i p_{cv}^{n+1,k+1}} \right) \quad (3.29)$$

9. The rigid constraint force is removed from the velocity field.

$$u_{i,cv}^{**,k+1} = \frac{1}{\rho_{cv}^{n+1}} \left(u_{i,cv}^{*,k+1} - \Delta t f_{i,cv}^{n+1,k} \right) \quad (3.30)$$

10. The rigid-body motion is computed a $t = n+1$ using the previously computed

solution of the flow.

$$\mathbf{U}_M^{RBM,k+1} = \mathbf{U}_M^{T,n+1,k+1} + \Omega_P^{n+1,k+1} \times \left(\mathbf{X}_M^{n+1} - \mathbf{X}_P^{n+1}\right) \tag{3.31}$$

11. The extra force term to enforce rigidity in the objects is computed.

$$F_{i,M}^{n+1,k+1} = \rho_M^{n+1} \frac{U_{i,M}^{**,k+1} - U_{i,M}^{RBM,k+1}}{\Delta t} \tag{3.32}$$

12. With the last step a new velocity field is obtained taking into account the particles in the domain and the rigidity constraint associated to the particles. The flow is then solve again from step 3 in order to ensure convergence of the velocity field.

$$F_{i,M}^{n+1,k+1} = \rho_M^{n+1} \frac{U_{i,M}^{**,k+1} - U_{i,M}^{RBM,k+1}}{\Delta t} \tag{3.33}$$

13. Finally the particles velocities and positions are reset with the newly computed values.

$$U_{i,M}^{n+1} = U_{i,M}^{T,n+1,k+1} \tag{3.34}$$

$$\Omega_{i,M}^{n+1} = \Omega_{i,M}^{n+1,k+1} \tag{3.35}$$

$$X_{i,M}^{n+3/2} = X_{i,P}^{n+1/2} + R_{ij}\left(X_{j,M}^{n+1/2} - X_{j,P}^{n+1/2}\right) + U_{i,M}^{T,n+1}\Delta t \tag{3.36}$$

Apte et al. [15] present an error analysis based on the simulation of a simple

Taylor vortex case. This case is relevant for an error analysis since an analytical solution exists for the pressure and velocity fields, therefore it is straight forward to compute the error generated by the code. In order to test both the flow solver and the interpolation of the material points onto the background mesh, several cases are run with and without an immersed object at several levels of grid refinement.

In the case where an immersed object is injected in the domain the analytical solution of the Taylor vortex is applied to each material volume so that the error in that region will come from the interpolation between the material points and the background grid. This allows to test the interpolation method. Apte et al. [15] show that the error both for the pressure and the velocity field converges with a second order accuracy. However, in the case where an immersed object is present the error for the velocity field increases by an order of magnitude.

Chapter 4 – Validation

This section presents several test-cases necessary to ensure that the code is working properly and gives reliable results. In order to be confident in the ability of the code to solve both single-phase and two-phase flows several simulations are run and compared with available results in the literature: (i) flow in a microchannel, (ii) flow over a fixed cylinder, (iii) flow over an oscillating cylinder, (iv) flow over a stationary sphere, (v) sphere rising in an inclined channel and (vi) equalizing flow rates in the 3-channel geometry.

In addition to ensure the global accuracy of the code, these test cases are relevant towards the goal of this work, and ensure that every aspect of the simulation can be properly resolved by the code.

4.1 Microchannel case

The first test case is a simple flow in a 3D channel. This case has been presented by Qu et al. [20]. Flows in a micro-channel at different Reynolds numbers ($Re_{ch} = 196$, $Re_{ch} = 1021$ and $Re_{ch} = 1895$) have been simulated. Velocity profiles and pressure drops are used to compare simulation with the experimetal and numerical results presented in Qu et al. [20]. This case is also relevant to the goal of this work since it involves a microchannel with a high-apect ratio.

The geometry is composed of a channel with the following dimensions: $L_{ch} = 120\,mm$, $H_{ch} = 694\,\mu m$ and $W_{ch} = 222\,\mu m$. Two large plenums at the inlet and outlet of the domain ensure that the boundary conditions won't perturb the solution inside the channel. An illustration is shown in figure 4.1 and the dimensions of the geometry are summarized in table 4.1.

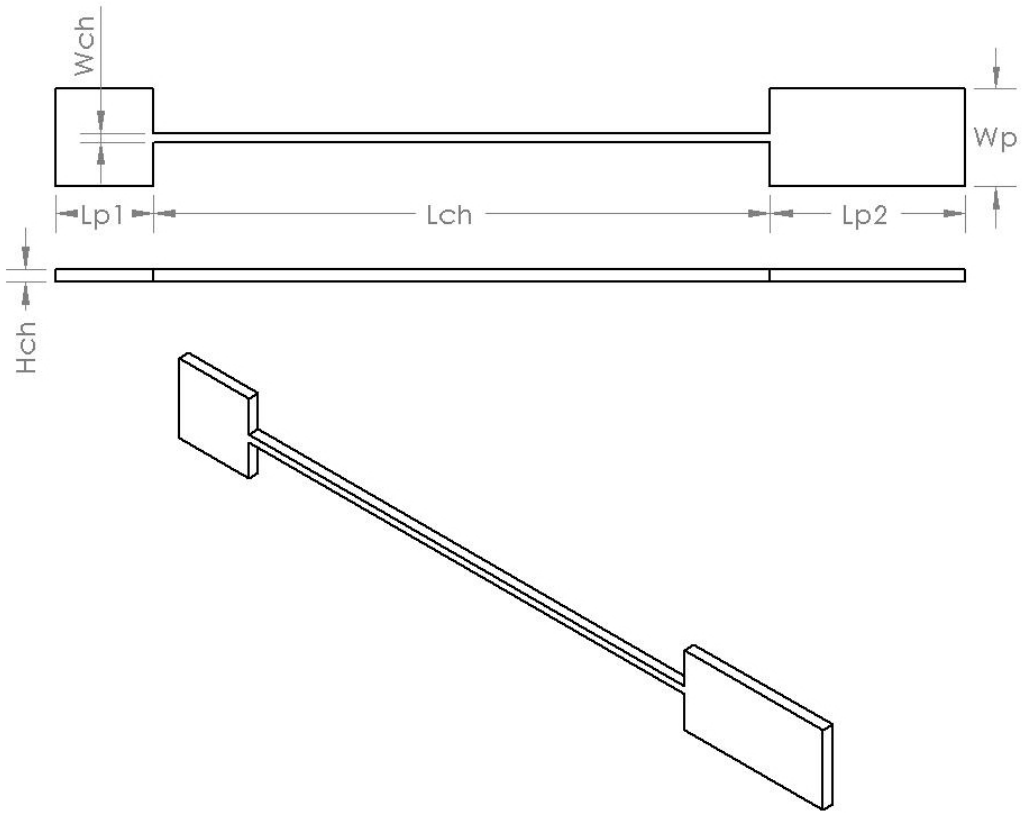

Figure 4.1: Schematic of the single channel geometry.

A fully developed velocity profile is applied at the inlet of the domain. The flow is simulated until the steady state is reached in the channel before collecting

Table 4.1: Dimensions of the single-microchannel geometry in $[mm]$.

Wch	Wp	Hch	Lp1	Lpch	Lp2
0.222	6.35	0.694	6.35	120	12.7

the data.

Due to the skewness and the aspect-ratio of the geometry it hasn't been easy to generate a grid to solve properly the flow. A non-uniform cartesian grid has been used in order to reduce the number of grid points and allow the flow to be solved in a reasonable amount of time. The grid inside the channel is uniform in the y and z directions and refined near the entrance and exit of the channel in the x direction. 320000 grid-points are used in the channel only, 40 grid-points are used in the y direction, 50 in the z direction and 160 in the x direction. The grid in the plenums is refined near the entrance and the exit of the channel in order to match the grid of the channel and have a smooth transition between plenum and channel. A total of 740000 grid-points are distributed over the entire geometry.

Figure 4.2 compares the velocity profile at different location inside the channel with numerical and experimental data. The parabolic profile is well achieved and a good agreement is obtained with the numerical results. Also the velocity profile agrees fairly well with the experimental data.

Figure 4.3 shows the velocity along the center line of the channel. A very good agreement is achieved with experimental data. Table 4.2 presents the pressure drop computed with the theoretical pressure drop. A good agreement is achieved for low Reynolds number (up to $Re_{ch} = 1021$). For $Re_{ch} = 1895$ the pressure

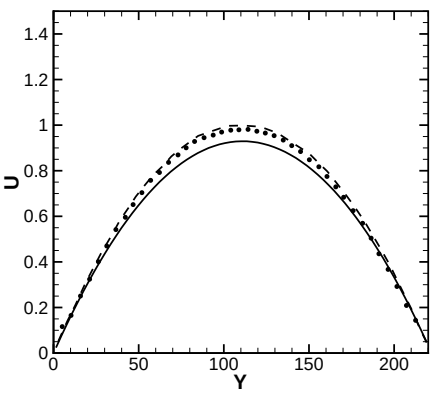

(a) $Re = 196, x' = 1\,cm$

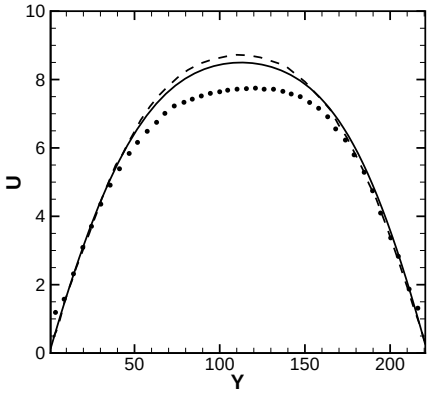

(b) $Re = 1895, x' = 1\,cm$

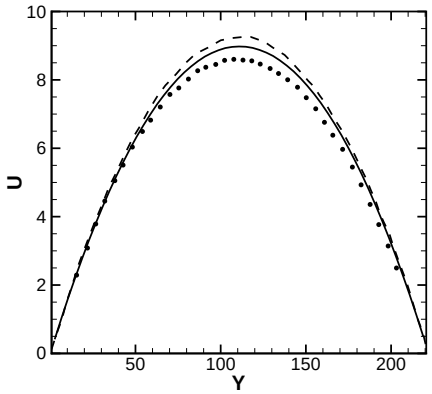

(c) $Re = 1895, x' = 10\,cm$

Figure 4.2: Velocity profiles in the center plane of the channel taken at $x' = 1\,cm$ and $x' = 10\,cm$ from the entrance of the channel. • shows the experimental data from [20], $- - -$ the numerical simulation from Qu et al. [20] and — the present study. The velocity is expressed in $[m/s]$ and the y location in $[\mu m]$.

Table 4.2: Comparison between theoretic and computed pressure drop through the channel.

Re_{ch}	Pressure drop in $[bar]$	
	Numerical simulation	Theory
196	**0.189**	0.200
1021	**1.09**	1.04
1895	**1.33**	1.93

drop is under-predicted by the simulation. This can be explained by the lack of resolution of the boundaries and by the strong effect of the entrance and exit of the channel. For this Reynolds number one would use a finer grid in order to capture the appearing turbulent effects.

4.2 Flow over a cylinder

In this section the results for flows over a cylinder at different Reynolds number are presented. These cases have been widely explored in the literature ([21, 22, 23]), therefore our data can be compared to what has been done in the past. These cases also provide a good case to test the behavior of the code with an immersed body in the domain. In order to compare our results with the ones already existing, drag and lift coefficients are computed for each case.

To compute the drag and lift forces (F_d and F_l) acting on the immersed body, a specific routine has been implemented. This routine defines a bounding box around an object and computes the fluxes crossing each face of the box. The balance of

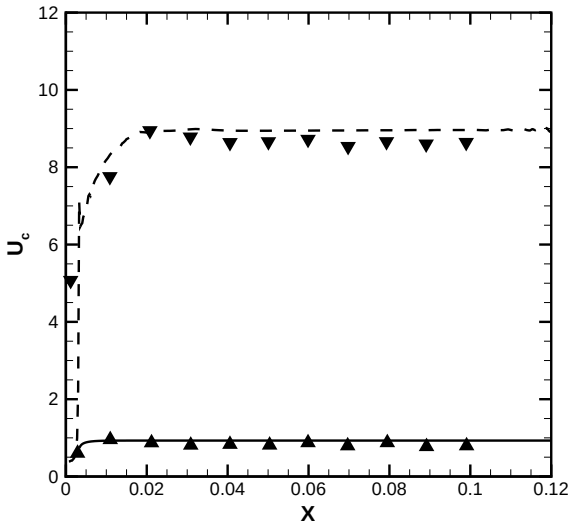

Figure 4.3: Velocity distribution along the central line of the channel. $Re = 196$: ▲ experimental data from [20], — present simulation; $Re = 1895$: ▼ experimental data, $- - -$ present simulation. Velocity is expressed in $[m/s]$ and the x location in $[mm]$.

these fluxes over the box added to the summation of the temporal change in velocity at each grid-point inside the box gives the drag forces (F_d, F_l and F_s). Equations 4.1 and 4.2 show the expression for the drag and lift forces and equations 4.3 and 4.4 respectively the drag and lift coefficients.The same approach has been used by Shu et al. [24]. These simulations help to validate this routine which may be used in computing the force acting on the bubbles in the microchannel geometry.

$$F_d = -\left\{\frac{d}{dt}\left(\int_\Omega \rho u d\Omega\right) + \int_S \left[\rho u \mathbf{u}\cdot\mathbf{n} + p n_x - \mu\left(\frac{\partial u}{\partial x_i} + \frac{\partial u_i}{\partial x}\right)\right] ds\right\} \quad (4.1)$$

$$F_l = -\left\{\frac{d}{dt}\left(\int_\Omega \rho v d\Omega\right) + \int_S \left[\rho v \mathbf{u}\cdot\mathbf{n} + p n_y - \mu\left(\frac{\partial v}{\partial x_i} + \frac{\partial u_i}{\partial y}\right)\right] ds\right\} \quad (4.2)$$

$$C_d = \frac{F_d}{0.5\rho_f U_\infty^2 d L_z} \quad (4.3)$$

$$C_l = \frac{F_l}{0.5\rho_f U_\infty^2 d L_z} \quad (4.4)$$

where ρ is the fluid density, u and v are respectively the x and y component of the velocity field $\mathbf{u}$, p is the pressure, $\mathbf{n}$ is the face normal vector, n_x and n_y are respectively its x and y components, μ is the viscosity of the fluid, Ω the 3D domain, S represents the faces of the volume Ω, d the diameter of the cylinder, U_∞ is the velocity of the flow far away from the cylinder and L_z is the size of the domain in the z direction.

For these simulations, 2 grids have been used. A coarse mesh using 245000 ($350\times350\times2$ respectively in the x, y and z directions) grid-points with 35 along the cylinder diameter (size of one element in the cylinder region: $\Delta = 1.14\times10^{-4} mm$)

has been used for the simulations at $Re_d = 40$ and $Re_d = 100$. A finer mesh with 423200 ($460 \times 460 \times 2$) grid-points and 100 points along the diameter has been used for higher Reynolds numbers $Re_d = 300$ and $Re_d = 1000$ ($\Delta = 4.0 \times 10^{-5}\, mm = 0.01d$). In both cases the grid is Cartesian and non-uniform. High resolution is achieved in the region of the cylinder. The mesh is stretched so that the grid is perfectly uniform in a region centered on the cylinder and $1.5d \times 1.5d$ large. Figure 4.4 shows the grid in the vicinity of the cylinder. The very fine mesh around the cylinder allows to perfectly resolve the shape of the immersed body. Also it allows us to solve the flow more accurately which is very important especially at higher Reynolds number. A large domain is used $40d \times 40d$ in order to avoid any influence of the boundaries. An Inflow and an outflow are used in the x direction, slip walls are applied in the y direction and periodic boundaries are used in the span-wise direction. For comparison Mittal et al. [21] uses non-uniform cartesian 385×105 mesh for $Re_d = 300$ on the same domain size, and Marella et al. [22] use a uniform cartesian 452×452 grid on a $30d \times 30d$.

At $Re_d = 40$ there is no shedding but a recicurlation bubble is created in the wake of the cylinder as shown in the figure 4.6. Ye et al. [25] show that the length of the recirculation bubble should be $\frac{L_w}{d} = 2.27$. The present study shows $\frac{L_w}{d} = 2.24$, so a very good agreement is achieved with the existing references. The drag coefficient presented in figure 4.5a also presents an excellent agreement with the literature as presented in the table 4.5. Note that no lift coefficient history is presented on figure 4.5a since for this low Reynolds number the perfect symmetry of the flow around the cylinder doesn't produce any excess of lift force in one

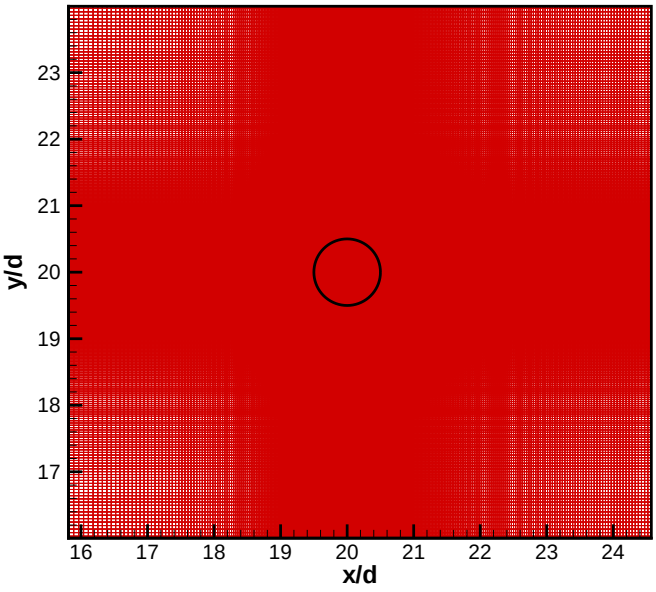

Figure 4.4: Non uniform grid employed around the cylinder for the simulation at $Re_d = 300$. The center of the cylinder is located at $x/d = 20; y/d = 20$.

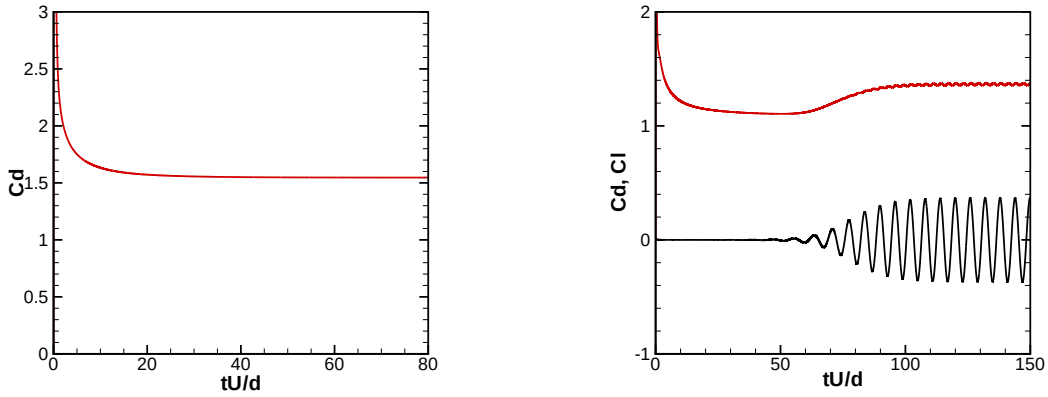

(a) $Re_d = 40$ (b) $Re_d = 100$

Figure 4.5: Drag and lift coefficients history for $Re_d = 40$ and $Re_d = 100$.— shows the drag coefficient and — shows the lift coefficient.

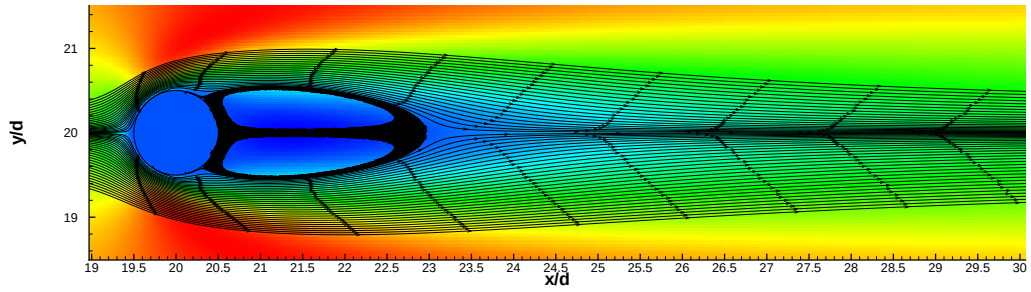

Figure 4.6: Velocity contour and streamlines around the cylinder for $Re_d = 40$ using the coarse mesh.

direction. In this case the lift coefficient is equal to 0 all the time. The perfect symmetry of the flow can be observed on figure 4.6. This figure presents the contour of the velocity around the cylinder and the streamlines. It shows the symmetric high velocity region above and underneath the cylinder, the recirculation bubble in the wake of the cylinder and the symmetric pattern of the streamlines around the cylinder.

At $Re_d = 100$ vortex shedding appears. This can be seen through the shape of the lift and drag coefficients. The oscillations presented by the two signals are characteristic of vortices shedding from the cylinder. From this oscillation the Strouhal number can be calculated. The result for $Re_d = 100$ and $Re_d = 300$ are presented respectively in table 4.3 and 4.4.

Table 4.3: Strouhal number for $Re = 100$

Study	Mesh	St
Current	coarse	0.165
Mittal et al. [21]	-	~ 0.166

Table 4.4: Strouhal number for $Re = 300$

Study	Mesh	St
Current	coarse	0.205
Mittal et al. [21]	-	~ 0.21

Table 4.5: Drag coefficient C_d for flow over a cylinder.

Study	Mesh	Re_d			
		40	*100*	*300*	*1000*
Current	coarse	1.54	1.35	-	-
	fine	-	-	1.375	1.48
Body fitted grid		1.547	1.336	1.377	1.44
Mittal et al. [21]		1.53	1.35	1.36	1.45
Marella et al. [22]		1.52	1.36	1.28	-
Henderson et al. [23]		1.54	1.35	1.37	1.51

Figures 4.7 show the vorticity contour lines for the z component of the velocity. Qualitatively the vorticity contours match very well with the previous simulation. No quantitative estimation is given, however the range in vorticity for $Re_d = 100$ goes from $-815\ s^{-1}$ to $845\ s^{-1}$ and for $Re_d = 300$ from $-5100\ s^{-1}$ to $6339\ s^{-1}$ in these simulations. The magnitude of the vorticity at higher Reynolds numbers is greater compared to lower Reynolds numbers. The figures also show a reduction in the size of the wake (before the vortices detach from the cylinder). With higher Reynolds number, vortices are shed sooner at higher frequency and become circular earlier. This is consistent with what has been observed in previous studies.

Figure 4.8 presents turbulence statistics in the wake of the cylinder at $Re_d = 300$. These statistics have been collected once a steady regime has been achieved,

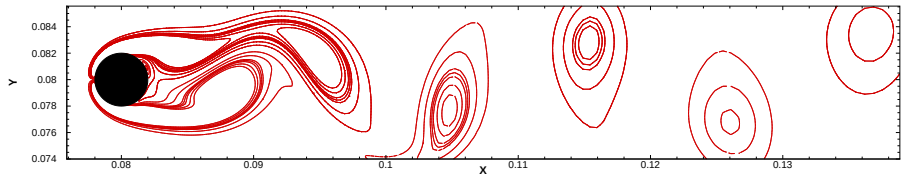

(a) $Re_d = 100$

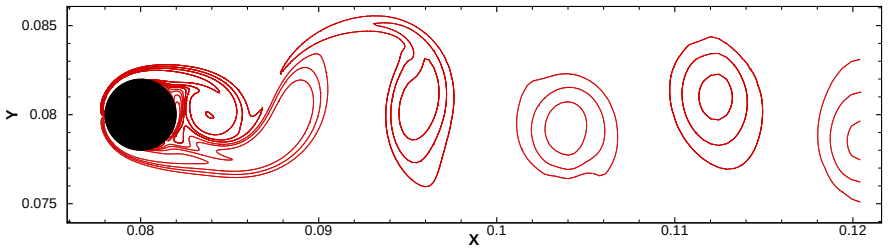

(b) $Re_d = 300$

Figure 4.7: Vorticity contour lines in the wake of the cylinder. $Re_d = 100$ (figure 4.7a) and $Re_d = 300$ (figure 4.7b).

then averaged over time. Figure 4.8 presents a comparison between the simulations using traditional body-fitted grid technique[1] and the simulation using the fictitious domain approach. A very good agreement is achieved between the two simulations for each parameter and at each location. The same statistics for the same case are presented by Kravchenko et al. [26]. Their results are not presented here for clarity of the graphs however a very good qualitative agreement is also achieved. Their simulations use a 3D domain to take into account the effect of 3D structures developing at higher Reynolds numbers which cannot be compared quantitatively with the present study since the simulations described in this dissertation are 2D. It has be shown by Kravchenko et al. [26] and Mittal et al. [27] that with the

[1]Simulation results through private communication with Justin Finn.

increase of higher Reynolds number 3D structures developing in the wake of the cylinder have a very strong effect on the flow. This, of course, cannot be captured in our simulation since it would require a full 3D domain which would involve a huge number of grid-points in order to fully resolved the phenomenon. Also such considerations are far beyond the purpose of the present simulations designed to validate the code.

4.3 Oscillating cylinder

For the second test case, a periodic oscillating cylinder in a fluid at rest is simulated. This case has been used throughout the literature to test the accuracy of immersed boundary techniques as in Kim et al. [28]. Experimental data are available from Dütsch et al. [29]. These 2 references are used to compare our results with.

A periodic oscillating cylinder can be characterized by 2 non-dimensionnal numbers: the Reynolds number $Re = U_m d/\nu$ and the Keulegan-Carpenter number $KC = U_m/fd$, where $U_m = 0.01\, m/s$ is the maximum velocity of the cylinder, $f = 0.2\, Hz$ the frequency of the oscillations, $d = 0.01\, m$ is the diameter of the cylinder and ν the kinematic viscosity.

The position of the cylinder in the x-direction is defined by the equation:

$$x_p(t) = -A_p \sin \omega t \tag{4.5}$$

where $x_p(t)$ is the location of the centroid of the cylinder in the x-direction and A_p is

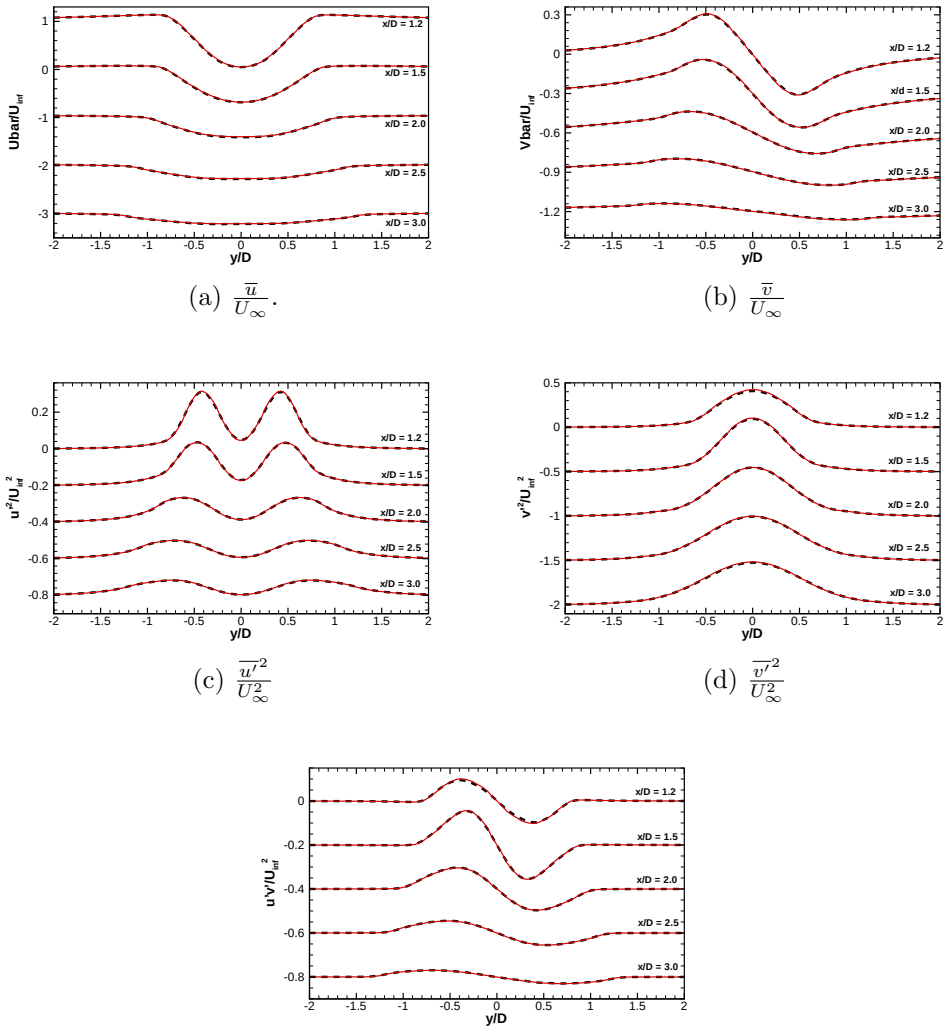

(a) $\frac{\overline{u}}{U_\infty}$.

(b) $\frac{\overline{v}}{U_\infty}$

(c) $\frac{\overline{u'}^2}{U_\infty^2}$

(d) $\frac{\overline{v'}^2}{U_\infty^2}$

(e) $\frac{\overline{u'v'}}{U_\infty^2}$

Figure 4.8: Turbulent statistics in the wake of the cylinder at $Re_d = 300$. The velocity profile is taken at 5 different locations in the wake of the cylinder. The data obtained with the fictitious domain technique are shown by — are compared with the results from the simulation performed using body-fitted grid − − −.

the maximum amplitude of the oscillation. The period of the oscillation is $\omega = 2\pi f$, therefore the Keulegan-Carpenter number can be rewritten as $KC = 2\pi A_p/d$. The parameters of the simulation are the same as the one used in the reference : $Re_d = 100$ and $KC = 5$.

The computational domain is a square box of $100d \times 100d \times d$ respectively in the axial, vertical and span-wise directions. The grid is refined and uniform in the region of motion of the cylinder and stretched towards the walls. The grid resolution in the cylinder region is refined so that 20 grid-points are always located along the cylinder diameter. Neumann boundary conditions are applied in the x and y directions. Initially the cylinder is placed at the center of the domain without any velocity, and the flow is at rest. The data are collected after the cylinder has gone through 10 cycles.

Figure 4.9 shows the comparison of the normalized velocity in the wake of the cylinder at 3 different angles of the cycle. Our results show excellent agreement with both experimental from Dütsch et al. [29] and numerical simuation data from Kim et al. [28].

4.4 Flow over a stationary sphere

To get an idea of the accuracy of the code in a 3D case, flow over a fixed sphere has been simulated. This case is also well documented since it serves as a base test-case in numerous validation studies for new codes. Even if the case seems pretty straight forward at first, it gathers several of the main issues that numerical techniques have

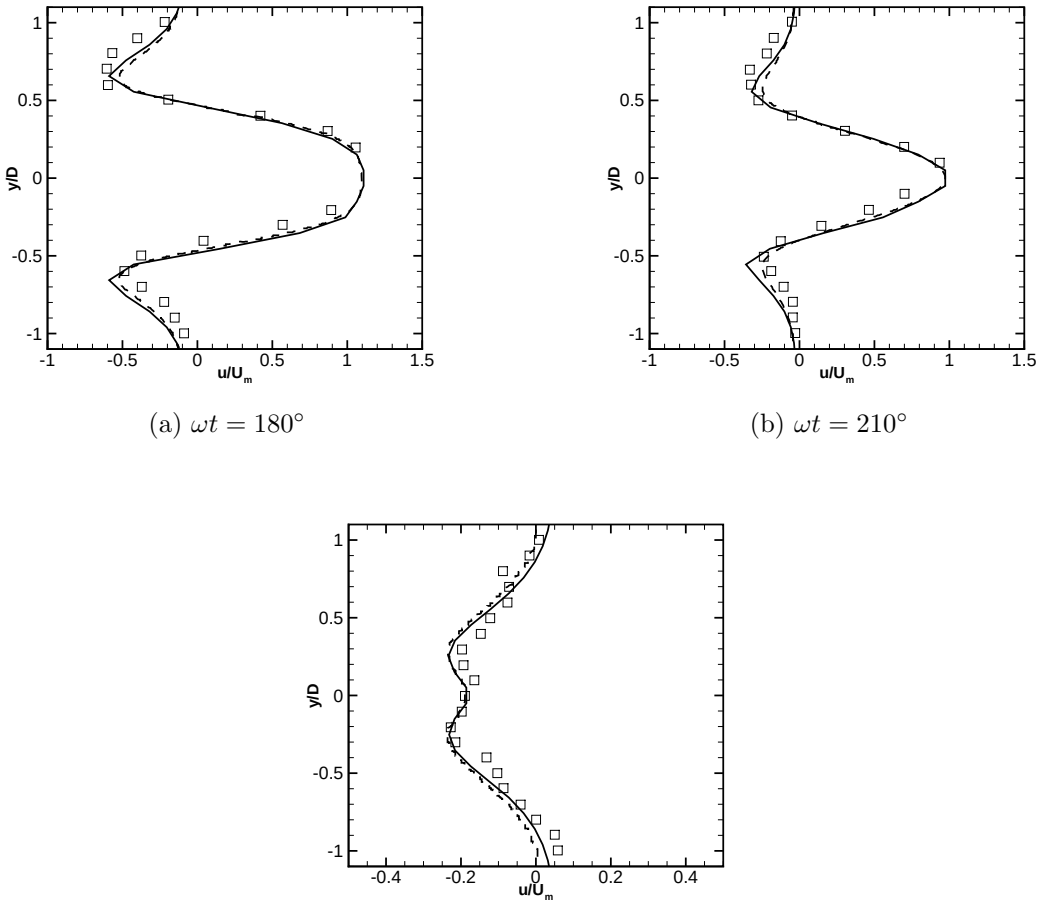

(a) $\omega t = 180°$

(b) $\omega t = 210°$

(c) $\omega t = 330°$

Figure 4.9: Normalized axial velocity (u/U_m) at three different phase position. The velocity is measured at a fixed x location ($x = -0.6d$) relative to the initial location of the particle center: □ Experimental data from Dütsch et al.[29]; — present simulation; − − − Numerical results from Kim et al. [28].

to face. First it requires a 3D domain which increases the total number of grid-points significantly and decreases the resolution of the grid. In comparison, it was possible to achieve 100 grid-points along the diameter of a cylinder in the previous cases, whereas in this case only 26 grid points are distributed along the diameter of the sphere. This has an effect on the solution of the flow in the boundary layer, at the surface of the sphere (region that needs to be resolved as well as possible).

Simulations are run at several Reynolds numbers in order to capture the different regimes. The transition between the different regimes can be identified based on the Reynolds number (Re_d) of the flow. Johnson et al. [30] describe the different regimes of the flow function of the Reynolds number. The first regime is steady and axisymmetric from $Re_d \approx 20$ to $Re_d \approx 210$. In this regime the flow presents a steady and symmetric wake. The next regime occurs for $210 < Re_d < 270$. Experimental results from Magarvey et al. [31] show that in this range the wake becomes non-axisymmetric but remains steady. Finally the last regime observed is the unsteady flow. This regime occurs at higher Reynolds number ($Re_d > 300$), typically from previous studies the transistion has been observed for $270 < Re_d < 300$. After the transition, vortices start shedding and 3D vortical structures appear.

To be able to compare this with the data available in the literature, the drag coefficient is computed for each Reynolds number. The domain is $15d$ in each direction, $d = 1.10^{-3}\ m$ is the diameter of the sphere. Figure 4.10 shows the grid used for the simulation. The sphere is located at $x = 5d$ and $y = z = 7.5d$. The flow is defined along the x axis in the increasing x direction. The grid used is $128 \times 128 \times 128$. The grid is non-uniform but it is refined and uniform around the

sphere forming a patch of $1.5d \times 1.5d \times 1.5d$. 26 grid points along a diameter of the sphere. For comparison Mittal [21] uses a domain of $16d \times 15d \times 15d$ and a grid of $192 \times 120 \times 120$ for their highest Reynolds number of 350 and Marella et al. [22] employed a $130 \times 110 \times 110$ mesh on a $16d \times 15d \times 15d$ domain. The fluid properties are $\rho = 1 kg.m^{-3}$ and the viscosity $\mu = 1.10^{-5} kg.m^{-1}.s^{-1}$. The sphere is not located exactly in the center of the domain. The x direction is slightly moved towards the inlet in order to increase the size of the domain in the wake. Also the density of grid-points is increased in the wake of the sphere in order to properly resolve the flow.

Table 4.6 shows the results for the drag coefficient compared with the results available in the literature. Our results are in very good agreement with the other simulations presented. The results also compare very well with the experimental data from Clift et al. [32]. A graphic representation of the results is presented on figure 4.11.

Table 4.6: Drag coefficient C_d for flow over a sphere at different Reynolds number

Study	Re					
	20	*50*	*100*	*150*	*300*	*350*
Current	**2.633**	**1.550**	**1.101**	**0.907**	**0.686**	**0.649**
Mittal (1999) [33]	-	1.57	1.09	-	-	0.62
Mittal (2008)[21]	-	-	1.08	0.88	0.68	0.63
Clift et al. [32]	2.61	1.57	1.09	0.89	0.684	0.644
Johnson et al. [30]	-	1.57	1.08	0.9	0.629	-
Marella et al. [22]	-	1.56	1.06	0.85	0.621	-
Kim et al. [34]	-	-	1.087	-	0.657	-

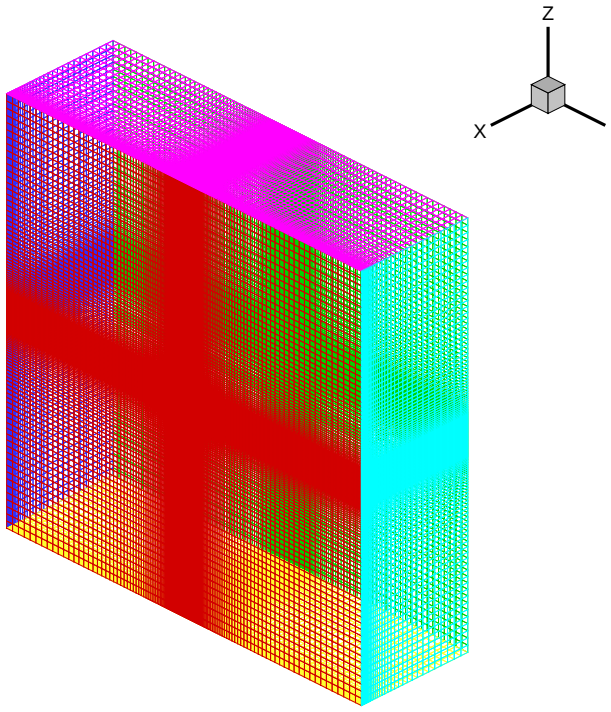

Figure 4.10: Grid used to study the flow past a stationary sphere. This shows the refinement around the sphere.

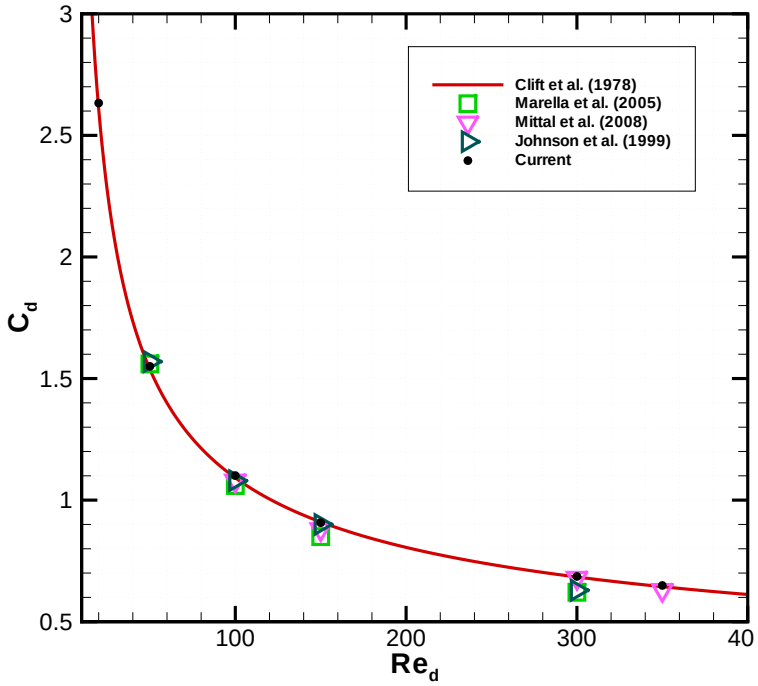

Figure 4.11: Comparison of computed mean drag coefficient for flow past a sphere with experimental and numerical data. • current study - — Clift et al. [32] - □ Marella et al. [22] - ∇ Mittal [21] - ▷ Johnson et al. [30]

Figure 4.12 presents the streamlines at all the Reynolds numbers simulated. Despite of the large number of streamlines, we can see that the flow stops being symmetric for $Re_d = 300$. The transition actually occurs for Reynolds number lower than 300. Figure 4.12e shows a quite perturbed wake which can be the sign of the unsteadiness. Overall, these patterns are in good agreement with the ones presented by Marella et al. [22].

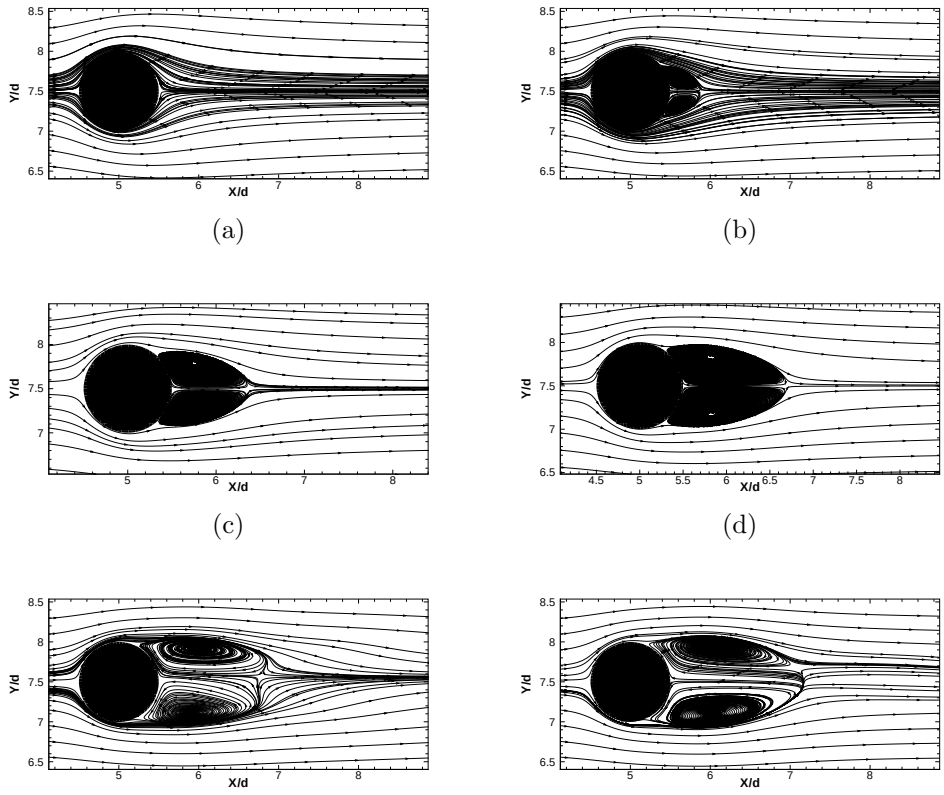

Figure 4.12: Streamlines past the sphere for different Reynolds numbers. Here are presented xy planes.4.12a $Re_d = 20$, 4.12b $Re_d = 50$, 4.12c $Re_d = 100$, 4.12d $Re_d = 150$, 4.12e $Re_d = 300$, 4.12f $Re_d = 350$.

Table 4.7: Comparison of key computed results for flow past a sphere with other experimental and numerical studies. x_c and y_c being the coordinates of the center of the recirculation bubble, d the diameter of the sphere and L_b the length of the recirculation bubble from the sphere.

	Re_d								
	50			100			150		
	x_c/d	y_c/d	L_b/d	x_c/d	y_c/d	L_b/d	x_c/d	y_c/d	L_b/d
current	0.617	0.204	0.382	0.757	0.287	0.866	0.327	0.33	1.2
Mittal [21]	-	-	-	0.742	0.278	0.84	0.31	0.3	1.17
Marella et al. [22]	-	-	0.39	-	-	0.88	-	-	1.19
Johnson et al. [30]	-	-	0.40	0.75	0.29	0.88	0.32	0.29	1.2
Taneda [35]	-	-	-	0.745	0.28	0.8	0.32	0.29	1.2

For the steady cases $Re_d = 50$, $Re_d = 100$, $Re_d = 150$ other key features of the flow can be observed and compared with references. Table 4.7 presents a comparison of the dimensions of the recirculation bubbles in the wake of the sphere. It presents the normalized x and y locations of the center (eye) of the recirculation regions and their normalized length. A very good agreement is obtained with the results available in the literature.

The results obtained for the steady regimes are in very good agreement with other references. The unsteadiness is observed for $Re_d = 300$ and $Re_d = 350$ in the streamlines plots (figures 4.12e and 4.12f). Figure 4.13 shows the evolution of the drag and lift coefficients for the unsteady case at $Re_d = 350$. The drag and lift coefficients are not oscillating but they are showing irregular small variations in time as shown by Mittal [21].

When it becomes unsteady, the flow in the wake of the sphere presents interesting structures. This structure can be extracted and visualized by plotting the vorticity (or enstrophy), however this method won't allow to visualize properly the actual vortical structures. In order to show the 3D vortical structures it has been shown that plotting the imaginary part of the eigenvalue of the velocity gradient tensor (λ) at each grid-point provides a nice and sharp representation of the vortical structure. This method is proposed in Chong et al. [36] and used by Mittal [33]. The analytical calculation details, available in Chong et al. [36], are quite straight forward, however in order to perform these operations efficiently on a large number of grid points the numerical library LAPACK [37] has been used. Chong et al. [36] explain that imaginary eigenvalues appear in the velocity gradient tensor

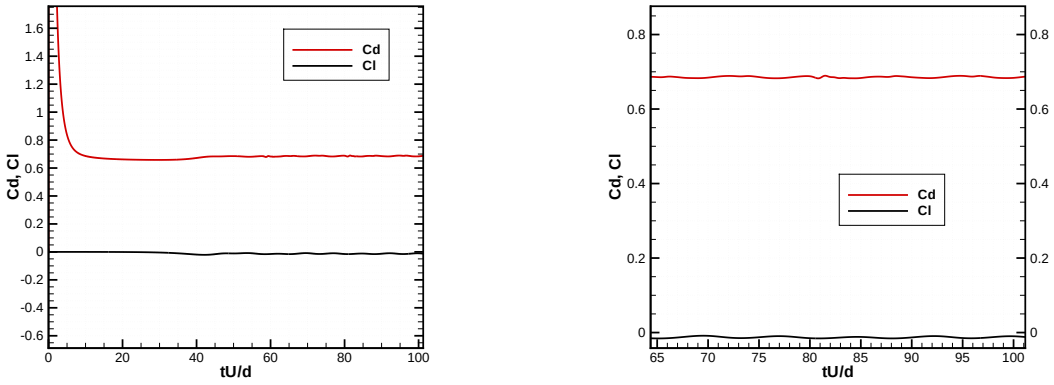

(a) (b)

Figure 4.13: Drag and lift coefficients for flow over a sphere at $Re_d = 350$. Figure 4.13a shows the drag and lift coefficient over the entire time; figure 4.13b shows the details of the variations in the temporal variations of the drag and lift coefficients. — shows the drag coefficient and — shows the lift coefficient.

where the rotation dominates over strain and the streamlines are circular.

Mittal [33] shows the iso-surface of λ for $Re_d = 350$. It is difficult to quantitatively compare the results with the ones presented in the latter paper because the intensity of the strength of the vortical structure is a function of the time when the data are collected. Also the structure shedding in the wake of the sphere is not stationary, rings are shed at a certain frequency. All these dependencies make it hard to be able to actually compare 2 structures at exactly the same time. However some characteristic features can be extracted from these structures.

Figures 4.14 show different views of the vortical structure represented by λ. Qualitatively the plots show very similar structures as shown by Mittal [33]. The three plots are taken at the same moment and they just present different point

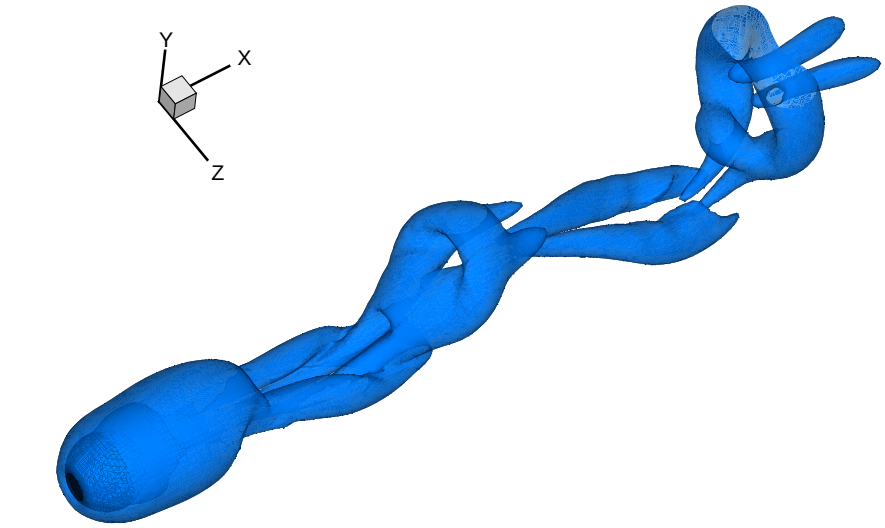

(a)

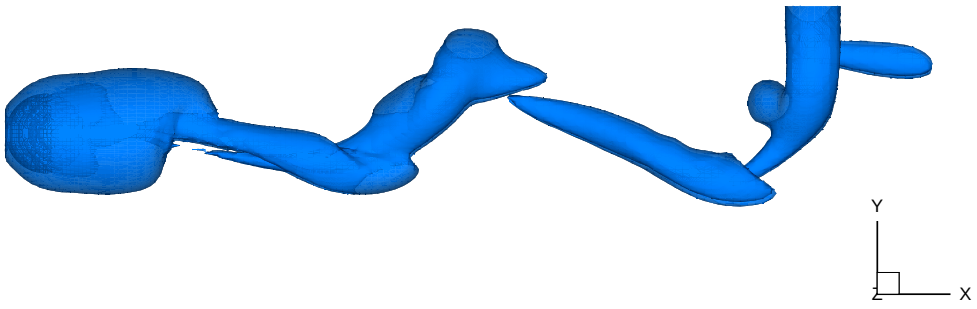

(b)

Figure 4.14

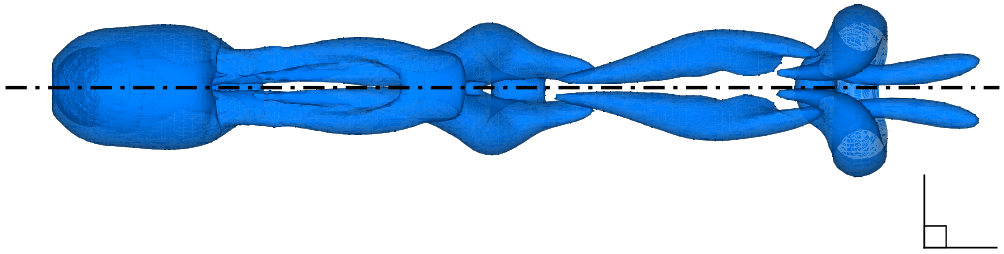

(c)

Figure 4.14: $\lambda = 0.008$ iso-surface for flow over a stationary sphere at $Re_d = 350$. The sphere is represented in black. Figure 4.14a shows a 3D perspective of the vortical structure. Figure 4.14b shows the view of the xy plane. and Figure 4.14c shows the view of the xz plane. The dash-dotted line shows the symmetry axis of the structure in this plane.

of view. This time is interesting because the birth of a vortex ring can be seen in the near wake of the sphere whereas a bigger ring is about to detach further in the wake which is comparable to what is shown in the reference. Another important feature is the symmetry axis shown in the xz plane. This feature has been observed experimentally, and this is actually a plane of symmetry for the entire vortical structure.

It should be noted that this particular case, in order to generate the data required to get this plot, the case has been re-run using LSRBM on a slightly different grid in order to get a larger range and a better resolution in the wake of the sphere.

The study of this 3D case has been very computationally demanding in terms of

resources but provides excellent results that compare very well with the available literature. These good results make us confident in the numerical approach and in the code.

4.5 Single sphere rising in an inclined channel

Another example of particle motion has been used to test the scheme: bubble rising in an inclined channel (Figure 4.15). As in the simulation, the bubble used is a rigid spherical particle. Such a bubble is introduced in an inclined channel. The density of the fluid is $\rho_f = 1115\, kg/m^3$ and the density of the particle is $\rho_p = 1081\, kg/m^3$. The viscosity of the fluid is $\nu = 3.125\, mm^2/s$. The Reynolds number Re_p^{Stokes} based on the Stokes settling velocity W is defined as :

$$Re_p^{Stokes} = \frac{2aW}{\nu} = \frac{4a^3}{9\nu^2}|\frac{\rho_p}{\rho_f} - 1|g \tag{4.6}$$

where $g = 9.82\, m/s^2$ is the gravitational acceleration, $a = 2\, mm$ is the diameter of the particle.

The domain is a rectangular box of $10\, mm$ in the x direction, $80\, mm$ in the y direction and $40\, mm$ in the z direction. The grid is cartesian and uniform over the domain $40 \times 320 \times 160$ grid points, respectively in the x, y and z directions so that $\Delta = 0.25 \times 10^{-3}\, m$.

The results of the simulation are compared with experimental and numerical data from [38]. The Reynolds number for this case is $Re_p^{Stokes} = 13.6$ and the

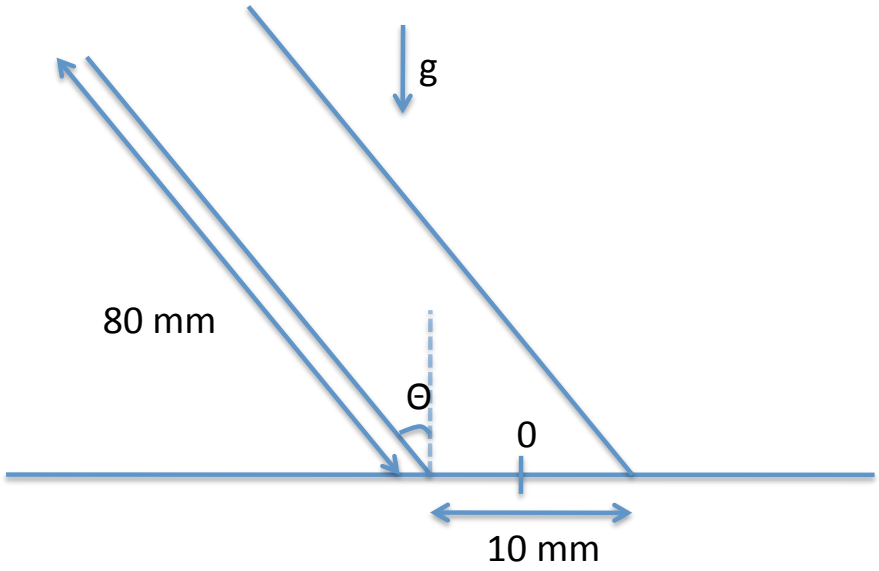

Figure 4.15: Geometry of the domain, for bubble rising in an inclined channel.

inclination angle is $\Theta = 8.23$ degrees. As shown in figure 4.16 the numerical simulation agrees very well with both experimental and numerical results. The bubble rises with buoyancy and gets closer and closer to the right wall of the domain. Ultimately the particle follows the right wall without touching it, keeping a very thin lubrication layer between the particle and the wall. Note that the results are presented on a vertical channel. The inclination of the channel is simulated by projecting the gravity acceleration vector on the x and y axis.

4.6 Equalizing flow rates

The last validation case uses the geometry and the features of the main simulation of the work presented in this thesis. The entire case will be deeply described in the

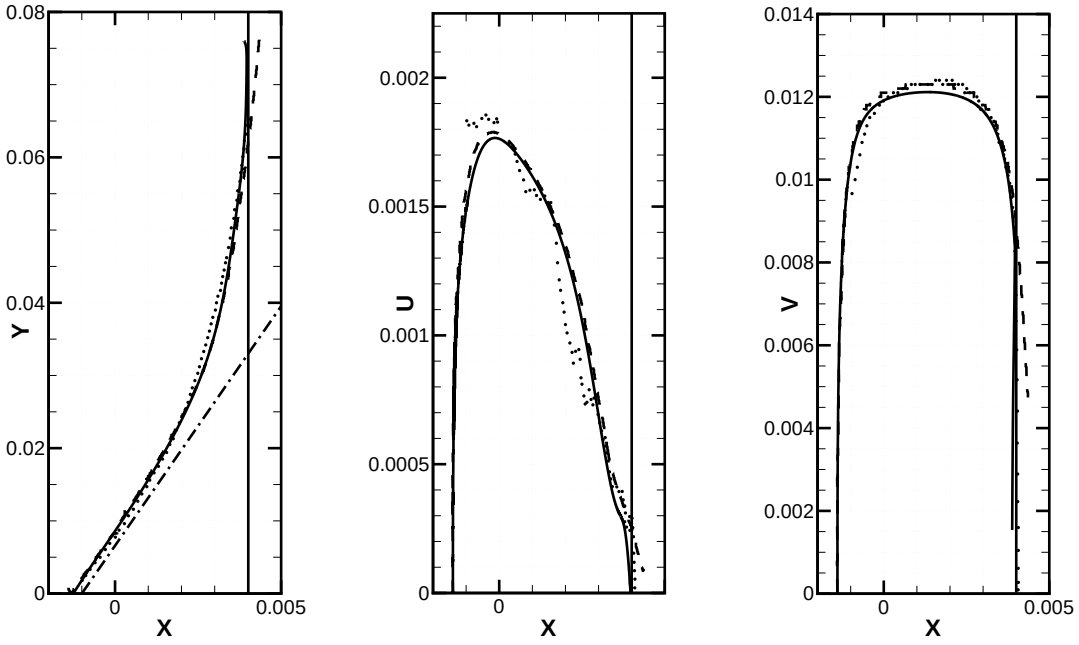

(a) (b) (c)

Figure 4.16: Results for bubble rising in an inclined channel. Comparison of experimental • and numerical simulations − − − [38] with the current simulation —. 4.16a shows the particle trajectory inside the domain (the −.− line shows the initial trajectory due only to the effect of gravity), 4.16b the velocity of the particle in the lateral direction and 4.16c the velocity on the vertical direction. The particle position is expressed in $[m]$ and the velocities are expressed in $[m/s]$.

next chapter. In this particular simulation, the ability of the controller and CFD code to communicate in order to equalize the flow rate in each channel is tested by trying to equalize the mass flow rate in the three channels of the geometry by acting on the valve. Due to the parabolic profile of the inflow and the non-symmetric geometry, the mass flow rate in each channel is slightly different. This offers a good case to test the controller and the communication between the CFD and the controller codes. Since the mass flow rate is imposed at the inlet, the amount of fluid entering the geometry is known. Hence, without any bubble in the geometry, the controller regulates the flow in each channel to achieve exactly the same mass flow rate in each channel.

The geometry, boundary conditions, and the grid are detailed in the next section. The steady state is achieved in the geometry keeping the valves fully opened. Then the controller is activated in order to achieve the same mass flow rate in each channel.

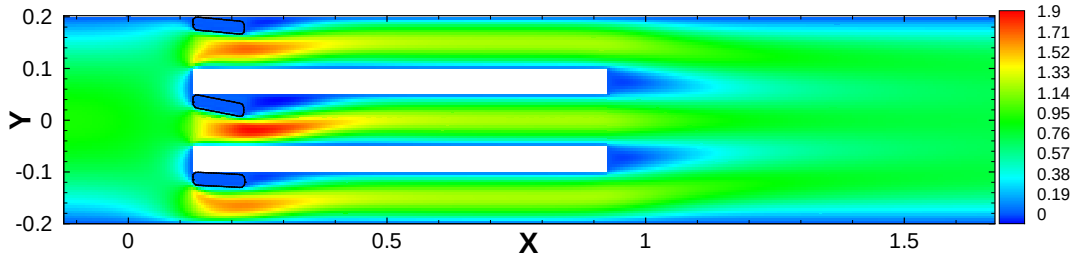

Figure 4.17: Velocity contour in the 3 channel geometry when steady state is achieved and mass flow rate equalized in each channel.

Figure 4.17 shows the velocity contour of the fluid inside the geometry once the

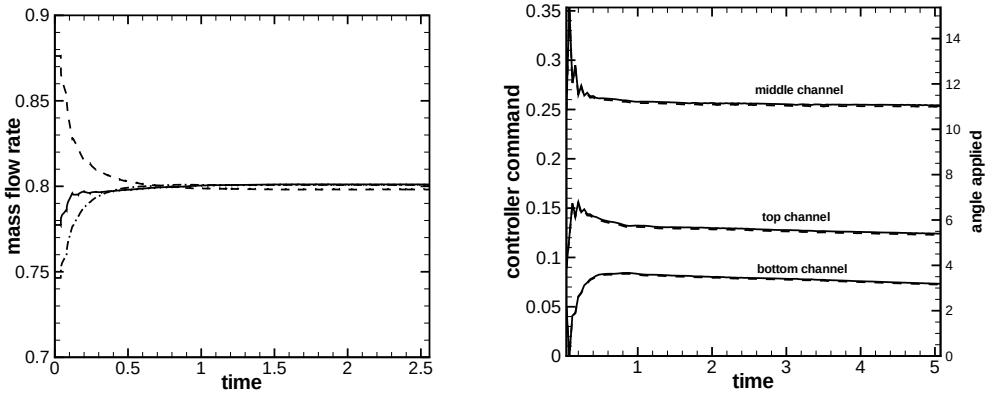

(a) Velocity history in each channel

(b) Controller output history correlated with angle applied to each valve.

Figure 4.18: — shows the data for the top channel; − − − middle channel; -.- bottom channel. The mass-flow rates are expressed in $[mg/s]$ and the time in $[ms]$.

steady state has been achieved and the flow equalized by the controller. The closing angle of the center channel is more important than in the other channels since, due to the inlet boundary condition and the asymmetry of the geometry (with valves), this is where the flow rate tends to be the largest without any action.

Figure 4.18a shows the mass flow rate history in each channel. At the beginning the mass flow rate is very different in each channel; it is maximum in the center channel. By acting on the valves the controller partially closes the channels, reducing the flow rate in the center channel in order to increase it in the top and bottom channels until all the three channels reach the same mass flow rate. Compared to the theoretical value the maximum error observed once the steady state is achieved is around 0.16%. The maximum amplitude of the difference between the mass flow

rates in the each channels is on the order of 0.12%.

Figure 4.18b shows the history of the controller decisions. The output of the controller is correlated to the closing angle applied to each valve. The maximum closing angle is used for the valve of the middle channel, then the top channel and finally the bottom channel.

Chapter 5 – Microchannel simulation

The code has been extensively validated for the simulations described in this chapter. The flow through three connected parallel microchannels has been simulated. The goal of these simulations is to look at the effects of bubbles appearing in the geometry and to simulate valves acting on the flow separately in each channel in order to flush the bubbles out and to restore a nominal flow through the geometry. The simulation settings are first described then the results of the simulation involving an active control over the flow are presented.

5.1 Simulation settings

5.1.1 Geometry and model

As shown earlier in figure 1.1, the geometry we are looking at consists in three microchannels, and two plenums for the inlet and outlet. The dimensions of the domain are $1.8\,mm$ in the x direction, $0.4\,mm$ in the y direction and $0.025\,mm$ in the span-wise direction. The span-wise dimension is the same for all the geometry. The inlet plenum is $0.25\,mm$ and $0.4\,mm$ respectively in the x and y direction. The outlet plenum is $0.75\,mm$ and $0.4\,mm$ respectively in the x and y direction. The outlet plenum is longer than the inlet in order to avoid effects caused by the outflow boundary perturbing the flow inside the channels. The three channels are

exactly the same : $0.8\,mm$ in the x direction and $0.1\,mm$ in the y direction.

The grid is cubic and uniform in the three directions so that $\Delta = 0.005\,mm$, therefore there are five grid-points in the z direction over all the domain. In one channel there are twenty grid-points in the y direction and 160 grid-points in the x direction. Over the entire domain there are 128000 grid-points. Figure 3.2 shows the geometry and the grid used in 2 dimensions.

The boundary of the domain are inlet and outlet in the x direction, no-slip walls in the y direction and periodic boundaries in the z (span-wise) direction. Periodic boundary conditions are used in this case because the flow is mostly 2D due to the low Reynolds number and the geometry. No 3D effect in the z direction are expected. Periodic boundaries allow whatever crosses one of the boundary in the z direction to come back to the domain through the other symmetric boundary. Since no fluxes are expected in the z direction this is a fairly reasonable assumption that reduces the amount of grid-points without impacting on the the general behavior inside the domain.

At the inlet boundary of the domain a 2D fully-developped parabolic profile is applied, it is defined by equation 5.1

$$U_x = \frac{3}{2} U_p \left(1 - \left(\frac{y}{H}\right)^2\right) \tag{5.1}$$

where U_x is the velocity in the x direction, $\frac{3}{2}U_p$ is the maximum velocity at the center of the domain, y is the coordinate in the y direction and H is the size of the domain (inlet plenum) in the y direction.

In our simulation we have used $U_p = 0.6\,m/s$ so that the global mass flow rate entering the domain (in 3D), defined by equation 5.2 is $\dot{m} = 2.4\,mg/s$.

As mentioned earlier, due to the parabolic profile, the flow is more important at the center of the domain and in the center channel. Paragrah 4.6 shows the action of the controller over the flow in to regulate and equalize the flow rate in each channel.

$$\dot{m} = \int \rho_f U_x dA \tag{5.2}$$

with $\rho_f = 1000\,kg/m^3$ the density of fluid and A the area of the inlet.

5.1.2 Controller[1][2]

In these studies Model Predictive Control (MPC) is used to maintain consistent flow between the three channels. MPC is a type of control that uses a model to predict the future behavior of a system. This prediction is then used to choose appropriate control actions. MPC is a proven method in large scale plants. Its robustness and ability to handle constraints makes it a very powerful form of control. MPC is applied in this case because typical forms of control such as PID are difficult to implement on multiple input and output systems (In this system the valve positions are the inputs and the flow rate in each of the channels are the outputs). Until recently MPC had only been applied to slow system where a lot of computational power is available, but as microcontroller technology has improved

[1]Contribution through private communication with Chris Patton and Dr. John Schmitt.
[2]More details about the controller can be found in [2].

MPC has been applied to a much larger range of systems.

There are two primary stages in developing a MPC controller. The first stage is developing a model. The behavior of the microchannel system that we are dealing with is described by the Navier Stokes equations. Full nonlinear Navier Stokes equations cannot be solved explicitly, and computation of solutions is very computationally expensive. A model predictive controller that implemented this type of model would be unable to keep up with the performance of the system. The most standard implementations of model predictive control rely on the availability of a linear model.

To generate a linear model of this system, standard system identification techniques presented in [39] are used. System Identification works by stimulating the system with a binary white noise signal. The resulting output is used to generate the linear model that best maps the input signal to the output.

The second stage of MPC development is tuning. The prediction horizon is the distance that the controller predicts into the future and the control horizon is how far into the future the controller can modify the inputs 5.1. When the model predictive controller predicts the future behavior of the system it chooses the series of future control actions (valve positions) that minimizes a given cost function over the length of the prediction horizon. An example of a simple cost

$$J = vK_v + \Delta vK_{\Delta v} + eK_e \tag{5.3}$$

Where v is the valve position, Δv is the change in the valve position in one time

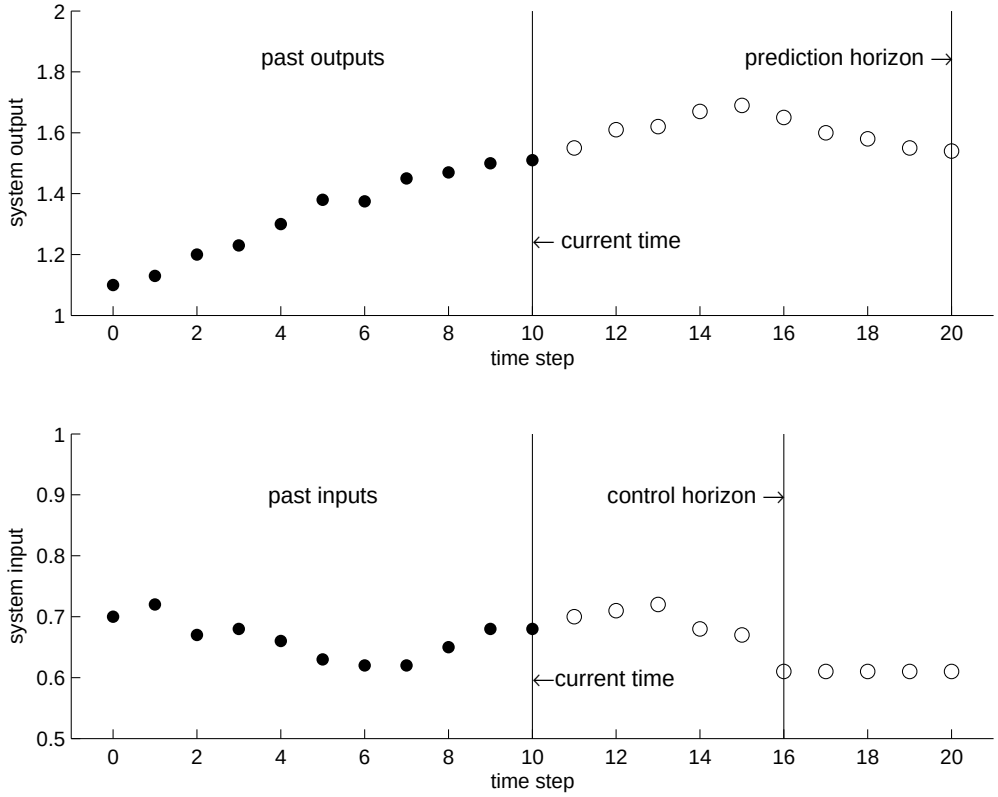

Figure 5.1: MPC Horizons

step and e is the difference between the flow rate and the desired flow rate. K_v, $K_{\Delta v}$, K_e are the respective weights. Shidhar and Cooper [40] develop a systematic method generating the desired tuning parameters. Their method provides an initial guess for weights and horizon lengths based on a few model parameters and a conditioning parameter. This method was used to develop the initial system parameters. After initial simulation these weights were modified to tune the system performance.

5.1.3 Valves and bubbles

In this simulation, valves have been added to control and regulate the flow separately in each channel. The angle of the valves is directly commanded by the controller (see paragraph 5.1.2 for details about the controller). The valves are defined using fictitious domain technique (described in chapter 3.1). They rotate following the orders from the controller, based on a percentage of the closing of each channel. Once the controller has decided a new configuration of the valves, the valves get to their new position. Since it's mostly a 2D simulation the shape of the valve is simply extruded in the span-wise direction.

As explained earlier, the bubble growth along the wall is not simulated in this work. Bubbles are represented as spherical rigid body. This assumption is valid for small Weber number. The Weber number is defined by:

$$We = \frac{\rho v^2 l}{\sigma} \tag{5.4}$$

where ρ is the density of the fluid, v the velocity, l the characteristic length (bubble diameter) and σ the surface tension. The Weber number represents the ratio of fluid inertia over the surface tension. If the Weber number is small enough the surface tension of the bubble is strong enough to sustain the inertia of the flow and therefore ensure that the bubble is not deformed by external forces. In our case that leads to a spherical shape for the bubble which is a valid assumption in the case of bubbly flow (diameter of the bubbles remains smaller than the height of the channel).

Another relevant parameter in this case is the Stokes number. It is defined by:

$$St = \frac{\tau_v}{\tau_f} \tag{5.5}$$

$$\tau_f = \frac{u_f}{L} \tag{5.6}$$

$$\tau_v = \frac{\rho D^2}{18\mu} \tag{5.7}$$

where τ_f and τ_v are respectively characteristic times of the fluid and of the bubble, D is the diameter of the bubble, μ the viscosity of the fluid, u_f the speed of the flow and L some characteristic length of the channel. In this case the calculated Stokes number is $St = 3.0 \times 10^{-4}$ which is smaller than 1. This indicates that the bubble won't have any effect on the flow. That means, as shown later, that the bubble, once released will flow through the channel at the same speed as the fluid without affecting the flow pattern or streamlines.

The bubble is injected very close to the wall, which is where it would grow if the bubble growth was actually simulated along the wall. Like the valves the bubble is simply extruded in the span-wise direction (forming a cylinder) which doesn't really matter since the flow looked at is mostly 2D (due to its low Reynolds number). The diameter of the bubble is $6 \times 10^{-2} mm$, so that the bubble plugs 60% of the channel height.The density ratio between the fluid and the bubble is $\rho_F/\rho_P = 10$ or $\rho_P = 100 kg/m^{-3}$. The density of the bubble remains pretty high ($\rho_P = 100 kg/m^{-3}$) compare to real vapor bubbles. This is due to convergence issues with the code at the time when these simulations have been set up. Considering the very low Stokes number the density of the particle doesn't play a significant role, so it

doesn't interfere with the general behavior of bubble or the flow.

The bubbles are injected close to the entrance of the channels. In the 2 bubbles case, the bubbles are injected at different x locations. The bubble in the top channel is injected at $x = 0.4\,mm$. In the bottom channel, the bubble is injected further into the channel at $x = 0.5\,mm$. Once the bubbles are injected they are artificially held fixed at their location. Bubbles held fixed will strongly perturb the flow in the channel. Figure 5.2 shows the flow without any action of the valves. Optimal flow is assumed when the flow is equalized in each channel. If a bubble, held fixed, is injected in the top channel. Figure 5.2a shows the velocity in the domain. It goes from $-0.23\,m/s$ in the wake of the bubble and the wake of the center valve to $2.24 m/s$ in the center channel, in the region below the valve. It can also be noticed that the velocity is pretty high ($\approx 1.9\,m/s$) above the the bubble itself. The mass flow rate in the unplugged channel has to increase in order to maintain the mass flow rate crossing the domain.

Figure 5.2b shows the pressure contour in the domain. The pressure drops slightly in the same way in both the middle and bottom channels but due to the bubble, the pressure drop is larger in the top channel, especially around the bubble itself. The pressure drop is slightly larger in the center channel. This is due to the parabolic inflow profile, more flow is forced through the center channel (compared to the bottom channel), therefore the pressure drop required to accelerate the flow in this channel is larger than in the bottom channel. It can be noticed regions of lower pressure, at the corner of the valves and above the bubble. These zones correspond to high velocity zone.

Figure 5.4 shows the pressure drop in each channel. As constated on the contour plot, the center and bottom channels are very close to each other after the initial pressure drop. The pressure at the entrance of the top channel is greater than in the others. The pressure drops with the bubble lower than in the other channel at the same location, towards the end of the channel the pressure is equivalent in each channel. The bubble then causes an abrupt drop in pressure of a magnitude close to $0.2\,bar$. Figure 5.3 presents the mass flow rate history inside each channel

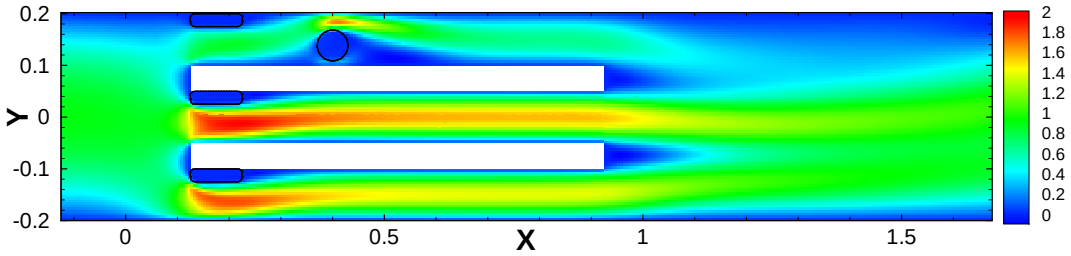

(a) Velocity contour; range from $-0.23\,m/s$ to $2.24\,m/s$.

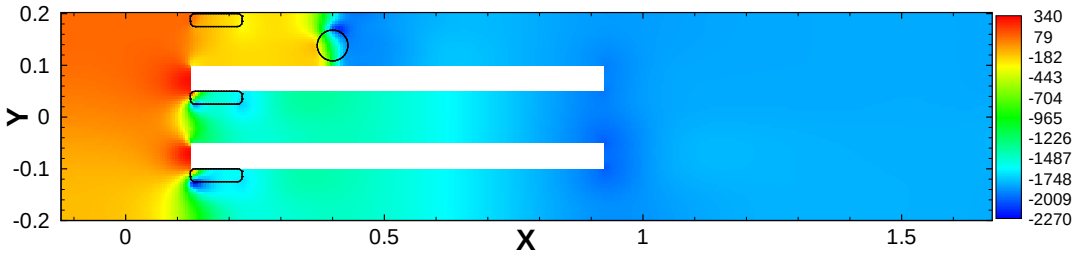

(b) Pressure contour; range from $-2617\,Pa$ to $340\,Pa$

Figure 5.2: Effect of a bubble held fixed in the 3 channels geometry on the velocity and pressure fields. The lengths are expressed in $[mm]$.

after the bubble has been injected. The mass flow rate is dropping in the top channel and increasing at the same time in the center and bottom channel, then

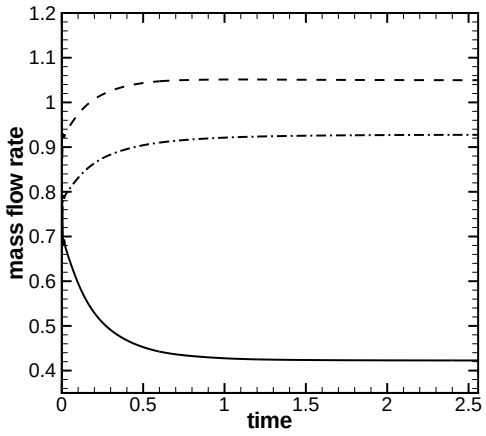

Figure 5.3: Mass flow rate history measured at the end of each channel. — shows the data for the top channel; − − − middle channel; -.- bottom channel. The mass flow rates are expressed in $[mg/s]$ and the time in $[ms]$.

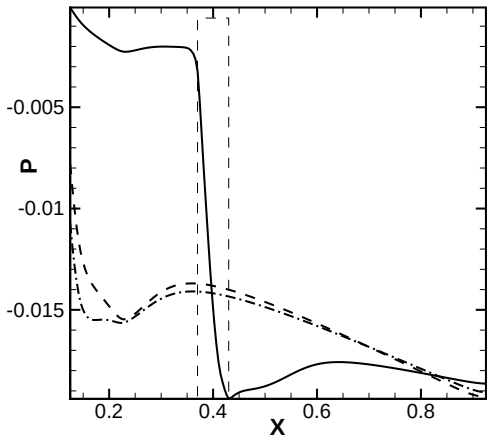

Figure 5.4: Pressure evolution along the center line of each channel. Note that the the pressure has been artificially set to 0 in the inlet plenum. The dashed rectangle represent the location of the bubble in the top channel. — shows the data for the top channel; − − − middle channel; -.- bottom channel. Pressure is expressed in $[bar]$ and location in $[mm]$.

pretty fast a new steady state is achieved. The flow has significantly been reduced in the top channel which could compromise its efficiency in case of heat exchange for example, where the flow rate in the channel is one of the key factor for a good heat exchange rate.

In a real microchannel with some heat apply at the walls, a bubble would form along a wall and grow perturbing the flow until the forces (surface tension, viscous forces) maintaining the bubble attached to the wall are too weak to sustain the force of the flow. To simulate the effect of the flow on the departure of the bubble, since the growth of the bubble is not taken into account in this simulation, the bubble is held fix against the wall and the force applied by the flow on the bubble is computed every time step. We define a threshold in the force of the flow from which the bubble gets released once the flow becomes strong enough.

In a system without an active controller there wouldn't be any way to modify the force acting on the bubble. The only solution would be to increase the mass flow rate in the entire domain to increase the force applied on the bubble so that it gets flushed. By acting separately on the flow rate of each channel it is possible to increase the flow rate in a specific channel for a short amount of time (just enough time to release the bubble). Figure 5.5 shows the range of force that can be applied on the bubble. The two most extreme cases have been looked at: all the channels fully opened allowing the flow to resolve itself, this configuration leads to the lower force applied on the bubble since as seen previously the mass flow rate drops significantly in the plugged channel; the other configuration is to force the entire flow through the plugged channel, this latter configuration obviously

corresponds to the maximum force situation.

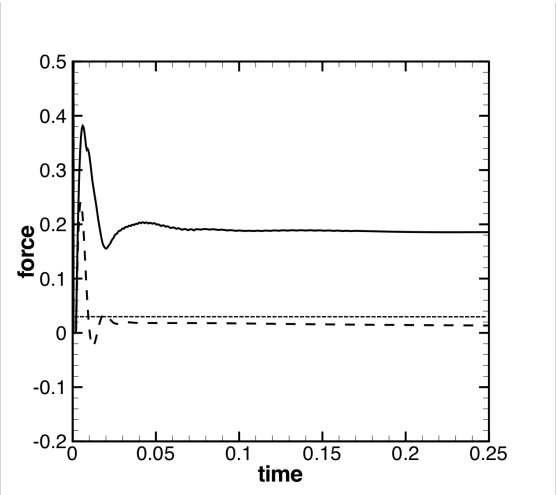

Figure 5.5: Temporal evolution of the total force acting on the bubble: – – – all channels are open, — the middle and bottom channel are completely closed. The forces are expressed in $[\mu N]$ and the time in $[ms]$. *The horizontal dashed line represents the threshold inertial force necessary to set the bubble in motion.*

The range of the forces that can be applied to the bubble goes from $0.013\,\mu N$ to $0.19\,\mu N$.

5.1.4 Sensors and communication between CFD code and controller

The CFD code is dumping the mass flow rate provided by two sensors in each channel (one probe is near the entrance of the channel and the other is located near the exit). A sensor is a plane (cross-section) which measures the mass flow-rate going through it at every time-step. The mass flow rate is then averaged over the section and normalized by ρ_f. The equalizing flow rate simulation presented in paragraph 4.6 can be used as a validation for the sensors, since once the equalized

regime is reached the sum of the mass flow rate captured by the sensors is equal to the theoretic mass flow rate entering the entire geometry through the inlet boundary.

It can be noticed that 2 distinct sensors are used in each channel and they both provide data to the controller. This has been designed in order to avoid confusion when the bubble is crossing one of the sensors. Since the density of the bubble is 10 times smaller than the fluid, the mass flow rate measured when a bubble crosses a sensor experiences sharp changes that are not relevant for the mass flow rate of the fluid. As soon as one of the sensors in one channel senses such a sharp transition, the controller uses the data from the other sensor. Since they are both located in the same channel the mass flow rate of the fluid is exactly the same, so it doesn't perturb the controller decision.

5.1.5 Flow regime

In the simulations presented in this study, even if the injection of 1 or 2 bubbles in the domain has a strong effect on the flow, the global flow regime remains unchanged. Different Reynolds numbers can be defined in this situation. The Reynolds number is defined by the following equation:

$$Re = \frac{\rho_f u_f l}{\mu} \tag{5.8}$$

where u_f is the velocity of the fluid. Several velocities can be used for the Reynolds number calculation based on either the maximum speed in the channel, or some kind of averaging. In the same way, the length l which can be based on the diameter of the bubble or some characteristic dimension of the domain like the hydrodynamic diameter (not appropriate here since it's a 2D case) or the height of the channel. After computing the different Reynolds number with the different parameters, it is found that it doesn't vary much following which value are selected.

For the steady-state without any bubble $Re_{ch} = 190$. For the case with a single bubble in the domain, the Reynolds number based on the diameter of the bubble the Reynolds number $Re_d = 155$. Finally for the 2 bubbles case, $Re_d = 170$. In each case, the Reynolds number remains fairly low, maintaining a laminar regime inside the domain which is often the case in flow through microchannels.

5.2 Results and full simulation

5.2.1 Single bubble simulation

For the complete simulation, the scenario is to introduce a bubble in a steady flow already achieved by the controller. The mass flow rate has been equalized so that the fluid flows at the same speed in each channel. Figure 5.6 presents the flow history in each channel. At the very beginning of the simulation the mass flow rate is $0.8\,mg/s$ for each channel. Then the bubble is injected, the mass flow rate drops in the top channel and increases in the two other channels as expected. The

controller detects the change in the mass flow rate and start closing the center and bottom channels until enough flow is forced to go through the plugged channel in order to release the bubble. As mentioned earlier, once released the bubble flows at the same speed as the fluid, therefore the controller just has to equalize the flow again in order to get back to the nominal equalized regime. The abrupt drop in the flow rate of the top channel corresponds to the bubble crossing the sensor as we talked about earlier, at that point the controller used the data provided by the sensor at the entrance of the channel otherwise it would dramatically affect the decision and the behavior of the controller. Figures 5.7a and 5.7b present the

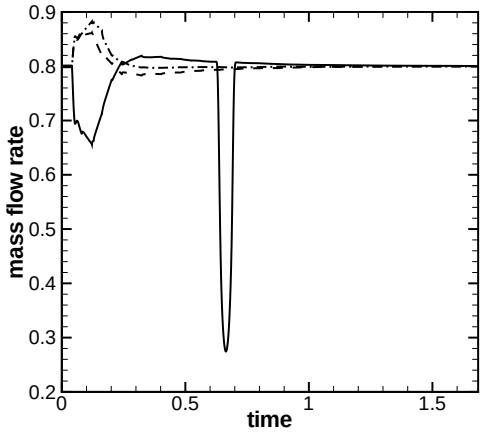

Figure 5.6: History of the flow in each channel with injection of the bubble at $t = 0.4\ ms$.— shows the data for the top channel; $- - -$ middle channel; -.- bottom channel. The time is expressed in ms and the mass flow rate in $[mg/s]$.

bubble velocity and location history during the simulation. At the beginning the velocity of the bubble is 0 since the bubble has yet to be released, then as expected the velocity in the x direction increases very rapidly to reach a final velocity. Note

that a spike appears at the beginning, when the bubble is released. This is most likely due to force calculation error when the bubble is suddenly released. Figure 5.7b confirms the story told by the velocity evolution, it shows that the bubble has a very small variation in the y direction inside the channel then once the bubble exits the channel, the bubble slows down in the x direction and goes toward the center line of the domain in y direction. The bubble history can be summarized by looking

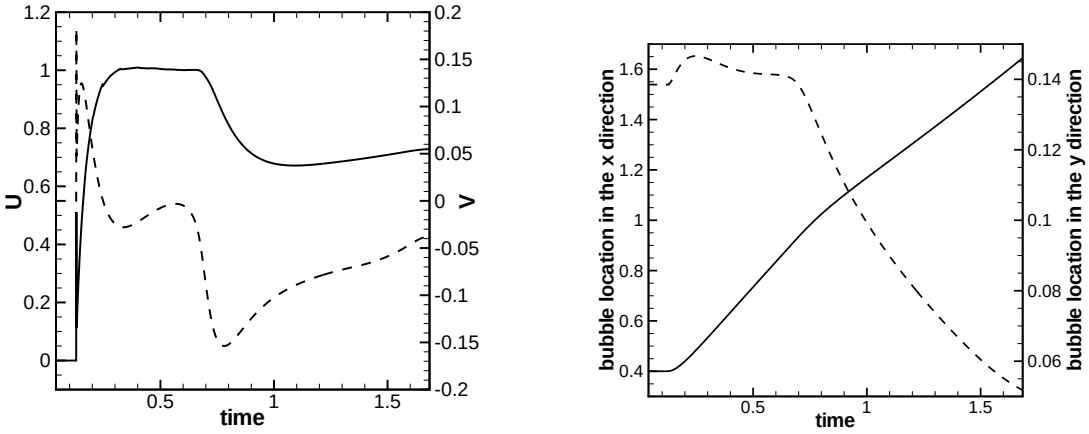

(a) Bubble velocity history

(b) Bubble location history

Figure 5.7: Velocity and location of the bubble history.— shows velocity and location in the x direction and $- - -$ shows velocity and location in the y direction. Time is expressed in $[ms]$, velocities are expressed in m/s and bubble locations in $[mm]$.

at the trajectory (Figure 5.8). The bubble has a fairly straight trajectory as long as it remains inside the channel. As soon as it exits the channel the bubble slowly goes down towards the center line of the domain ($Y = 0$). About the controller, figure 5.9 presents the evolution of the orders sent by the controller correlated with the angles applied as a consequence of the controller orders. As soon as the

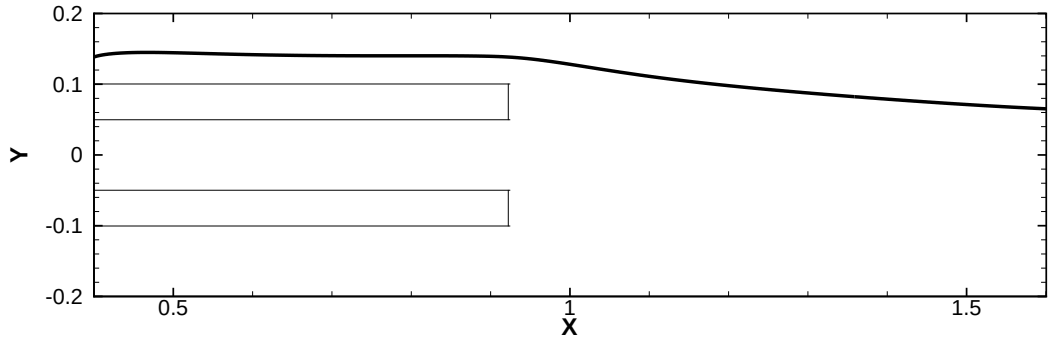

Figure 5.8: Bubble trajectory in the geometry. Locations are expressed in $[mm]$.

bubble is injected the controller starts closing the valves in the middle and bottom channel and fully opens the top channel. Once the bubble is released and doesn't present any resistance to the flow anymore, the controller starts equalizing the flow to resume a nominal flow inside each channel. A final value of the angle is achieved corresponding to a new equalized steady state.

5.2.2 2 bubbles simulation

The full simulation has been achieved using a single bubble in one channel. A simulation using two bubbles is now conducted. In this situation two bubbles in two separate channels are injected. This case is more challenging since the controller has now to take care of two bubbles. This simulation has been run with the same controller as in the previous case. The conditions remain the same. The 2 bubbles are injected at the same time in a stationary steady state achieved by

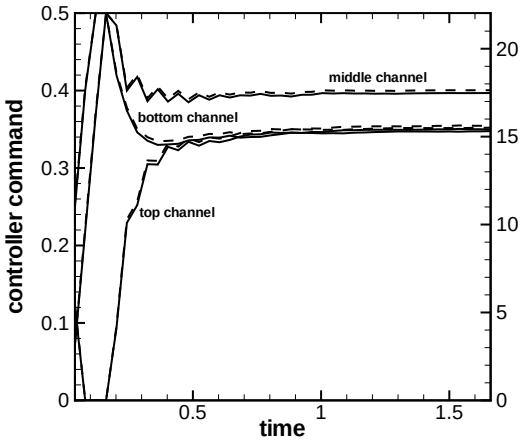

Figure 5.9: Controller output history correlated with angle applied to each valve.— shows the controller orders; $- - -$ shows the angle applied to the valves. Time is expressed in $[s]$, angles are expressed in degrees.

the controller. The force acting on each bubble is monitored and each bubble is released separately. The controller, by trying to achieve the same mass flow rate in each channel, increases the force acting on each bubble until the bubbles are released.

Figures 5.10 present the velocity contour at different stages of the simulation. They all show the effects of the valves and/or the bubbles on the flow. Figure 5.10a shows the velocity contour in the domain after the bubbles have been injected. Like in the one bubble simulation, the bubbles are injected when the steady state is achieved in the domain and the mass flow rate equalized in each channel. The presence of the bubbles increase the flow rate in the central channel and the highest speed region is located, as in the previous case, at the entrance, under the valve of the center channel. This is confirmed by figure 5.11 which shows that the lowest

pressure region is underneath the valve of the center channel. The velocity is also pretty high above the bubbles in each channel. This is due to the pressure drop caused by the bubbles.

The range of velocity is already pretty wide, it can be noticed that the lowest velocity is negative and is located in the wake of the valves where a recirculation bubble may occur. On the same figure, one can notice that the low pressure region is slightly tilted over the right side of the bubbles, this is due to the fact that the bubbles are not injected into the center of the channels, therefore more flow is going above the bubbles combined with the effect of the wall which tends to delay the lowest pressure point compare to a simple case of flow over a cylinder. Once the controller is turned on it detects the drop in the mass flow rate caused by the introduction of the two bubbles. Figure 5.13 shows the history of the mass flow rate in the three channels. It starts with a steady equalized mass flow rate until the bubbles are injected. The mass flow rate in the center channel is increased while the mass flow rate in the other two channels drops. The mass flow rate right before the controller starts acting for the first time is quite symmetric over the domain. This is summarized in table 5.1. The distribution of the mass flow rate is almost perfectly symmetric over the domain despite the fact that the two bubbles are not inserted at the same x location. The controller starts acting on the valves and starts regulating the mass flow rate in each channel. As shown in figure 5.10b the controller starts closing the center valve since it has detected a drop in the the mass flow rate in both the top and bottom channels. The valves of the plug channels are fully opened.

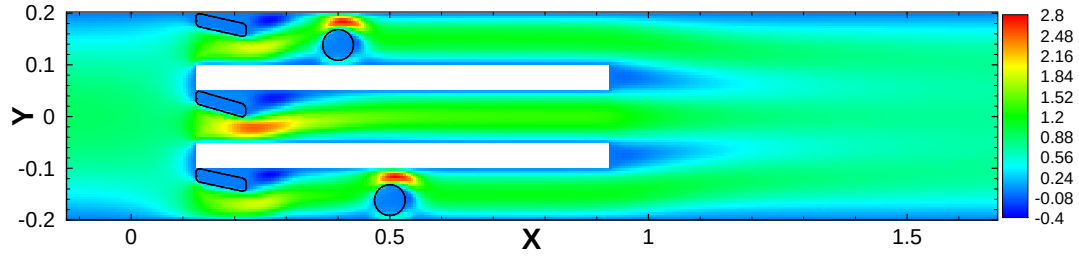

(a) Before action of the controller. The velocity range goes from $-0.31\ m/s$ to $2.79\ m/s$.

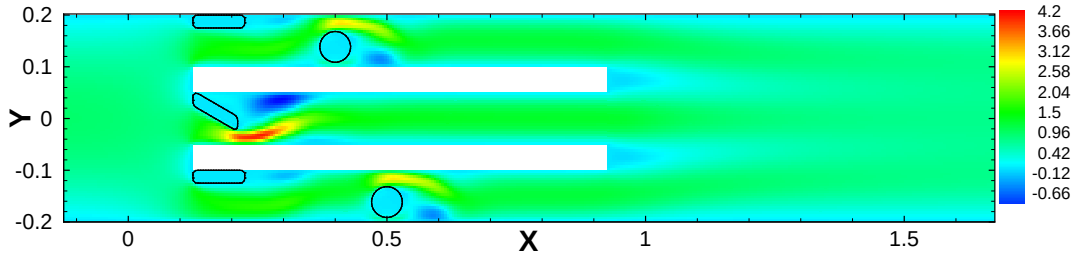

(b) After the controller has started acting n the valves.The velocity range goes from $-0.95\ m/s$ to $4.20\ m/s$.

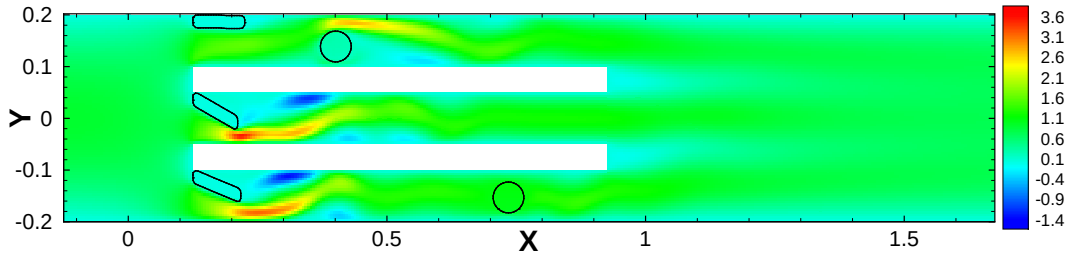

(c) After the first bubble has been released. The velocity range goes from $-1.36\ m/s$ to $3.71\ m/s$.

Figure 5.10: Velocity contour in the domain at different stage of the simulation with 2 bubbles in the domain. The lengths are expressed in $[mm]$.

The controller works by trying to equalize the flow. This is why the valves are reacting in a symmetric way. This might not be the best way to handle the situation because in this case in order to achieve the same mass flow rate it tends to send the same flow through the two plugged channels. A better way would be to shut two of the three channels in order to flush one bubble and then take care of the remaining one. In this case we assume that the flow forced through the plugged channels by the controller produces enough hydrodynamic force to flush the bubbles. The range of flow speed in figure 5.10b has increased. This is explained by the fact that naturally the flow would have a tendency to go through the center channel. However by closing it, the controller increases the velocity under the valve. The effect of the increased speed can also be seen in the recirculation zone in the wake of the center valve.

In that particular simulation the bottom bubble is released first since the force becomes large enough sooner as it can be seen on figure 5.18. As in the one bubble case a time is allowed for the force calculation to be effective. Figure 5.18 presents an initial spike that doesn't have any physical meaning, it just appears when the bubbles are injected. Once the bubbles are released the force acting on them drops close to 0 since the Stokes number is small enough so that the bubbles doesn't produce any effect on the flow. Figure 5.13 shows a sudden jump in the flow rate of the bottom channel when the bubble is released, at the same time the flow rate drops in the top channel (still plugged) since the bottom channel is fully opened and offers a wide open path to the flow. The release of the bottom bubble first can be explained by the fact that since the bubble is injected further

from the entrance of the channel, the flow is less influenced by the entrance effects. Figure 5.10c shows the flow after the bottom bubble has been released. Since it is not producing any perturbation in the bottom channel anymore the controller acts on the center and bottom valves in order to increase the flow through the top channel only. This corresponds to the single bubble case studied earlier. The release of the second bubble can be shown on the figure 5.13 when the mass flow rate suddenly increases in that channel. The controller regulates the flow in order to equalize the flow rate again in each channel. As before the spikes on the flow history plot correspond to the bubbles crossing the sensors used to determine the mass flow rate in each channel. This discrepancy is caused by the large density ratio between the two phases and doesn't affect the accuracy or the behavior of the controller. Figures 5.15 and 5.16 present the bubbles trajectory and velocity

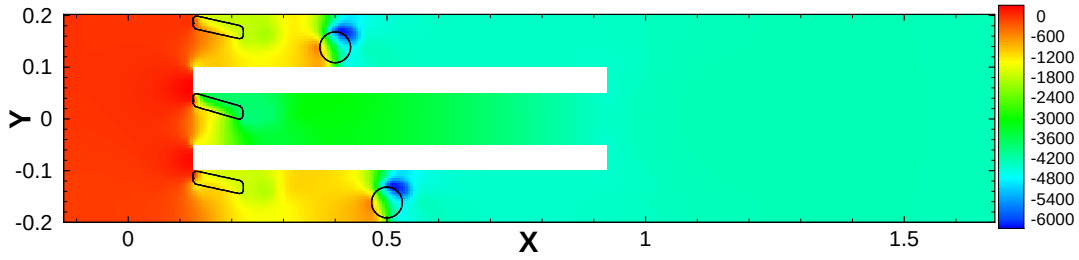

Figure 5.11: Pressure contour over the domain before the bubbles are released. The range of pressure of the domain goes from -4.1×10^{-2} *bar* to 3.29×10^{-3} *bar*. The lengths are expressed in $[mm]$.

history. The first set of plots (figure 5.15) presents the data for the bubble in the top channel. The initial flat line on the plots correspond to the time while the bubble remains fixed because it hasn't been flushed away yet. Once the bubble is

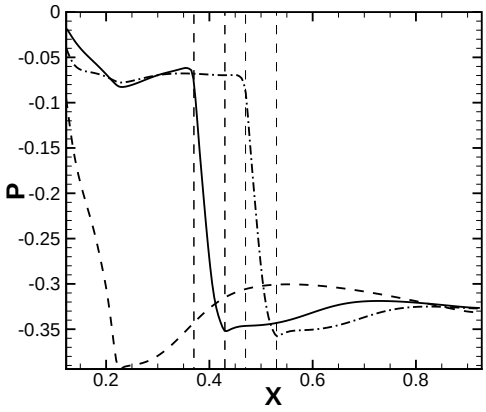

Figure 5.12: Pressure evolution along the center line of each channel for the 2 bubbles case. Note that the the pressure has been artificially set to 0 in the inlet plenum. The dashed rectangles represent the location of the bubbles in the top and bottom channels. — shows the data for the top channel; − − − middle channel; -.- bottom channel. Pressure is expressed in $[bar]$ and location in $[mm]$.

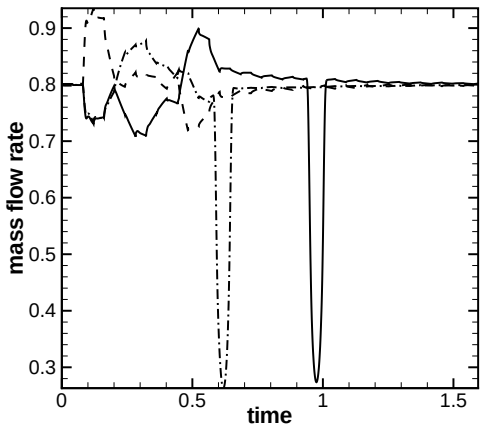

Figure 5.13: Mass flow rate history measured at the end of each channel. — shows the data for the top channel; − − − middle channel; -.- bottom channel. The mass flow rates are expressed in $[kg/s]$ and the time in $[ms]$.

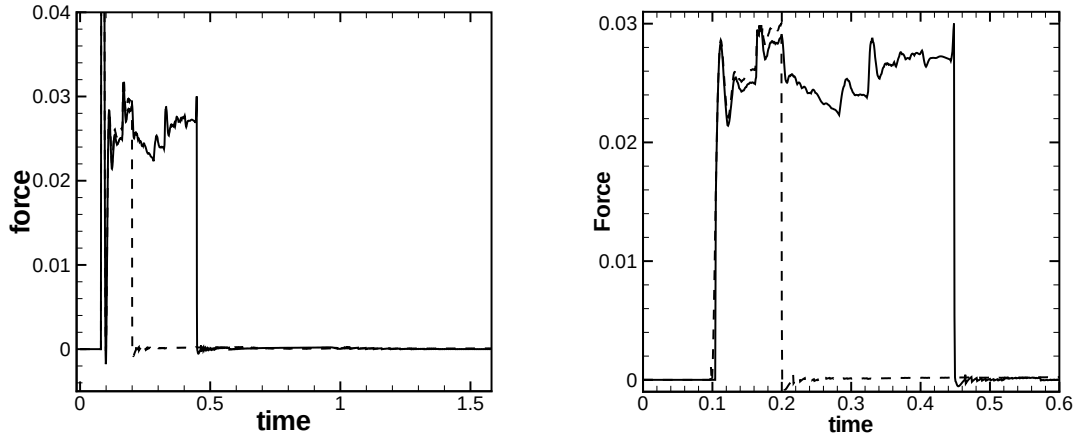

(a) (b)

Figure 5.14: History of the hydrodynamic force applied on each bubble. — shows the force history for the bubble initially in the top channel; − − − shows the force history for the bubble initially in the bottom channel. Time is expressed in $[ms]$, force is expressed in $[\mu N]$.

Table 5.1: Mass flow rate in the channels right before the controller starts acting in the 2 cases looked at.

	1 bubble	2 bubbles
time (in $[ms]$)	*0.053*	*0.098*
top channel	0.70	0.74
middle channel	0.85	0.91
bottom channel	0.85	0.75

released, a sudden jump occurs in the bubble velocity. Figure 5.15a shows the x and y components of the velocity history of the bubble. The u component of the velocity goes from 0 m/s to almost 1 m/s (it's terminal velocity) very rapidly, once again this is explained by the very low Stokes number. The bubble keeps roughly the same velocity until it exits the channel and enters the outlet plenum where its velocity decreases due to the decrease in the flow speed. This observation can be reenforced by looking at the figure 5.15b. The figure shows that the x component of the bubble location is linearly increasing. A slight change in its slope occurs when the bubble enters the outlet plenum. The amplitude of the v component is less significant. One can say that the bubble's trajectory remains fairly straight in the channel. This can also be seen on the figure 5.15b where the position of the bubble does not change while the bubble is in the channel then it drops as it enters the outlet plenum. This is due to the low pressure region along the vertical piece of wall between the top and middle channels (see figure 5.11).

Figures 5.16 present the same plots for the second bubble. This bubble is injected in the bottom channel and released first that's why the flat segment at the beginning of its plot is shorter than in the previous case. The same observations can be made concerning the behavior of this bubble. The x component of the velocity jumps from $0\,m/s$ to it's terminal velocity $\approx 1\,m/s$ as soon as the bubble is released. The velocity then decreases when it enters the outlet plenum. The bubble initially seems to position itself close to the center of the channel and then, according to figure 5.16b, slightly decreases in the channel until it exits the channel. Here for the same reason as previously but in the opposite direction, the bubble

is pulled up by the low pressure region just above the exit of the channel. Figure

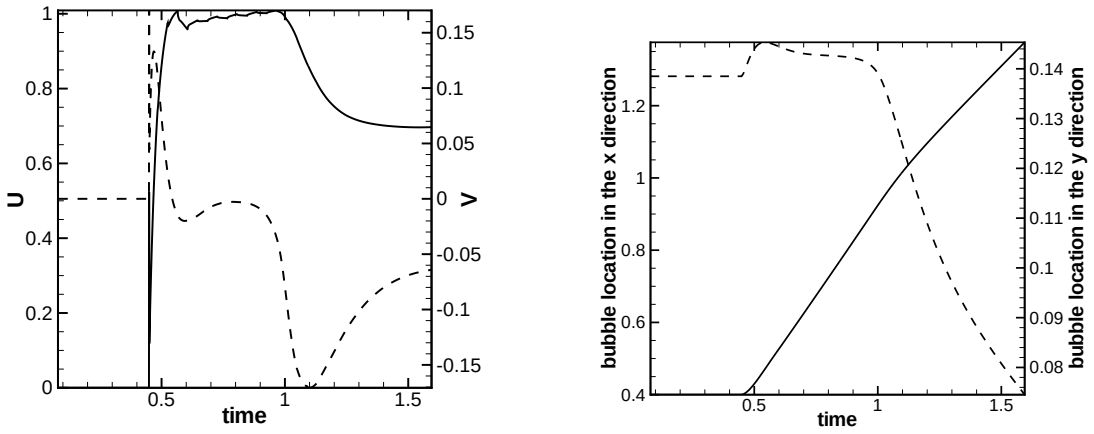

(a) Bubble velocity history

(b) Bubble location history

Figure 5.15: Velocity and location of the bubble history.— shows velocity and location in the x direction and $---$ shows velocity and location in the y direction. Time is expressed in $[ms]$, velocities are expressed in $[m/s]$ and bubble locations in $[mm]$.

5.17 summarizes the observation about the behavior conducted previously. One can notice that the bubbles tend to locate themselves towards the center of their respective channel as soon as they are released. This is due to shear force effect in the parabolic profile of a channel flow. It also shows the change in trajectory due to the entrance in the outlet plenum. The figure shows a shorter trajectory for the top bubble, this is due to the fact that the simulation has stopped as soon as the first bubble released hit the outlet boundary of the domain. Figure 5.18 shows the simulation from the controller perspective. This plot shows the history of the commands from the controller correlated with the angle applied by each valve. The controller is reacting to the change in mass flow rate over the

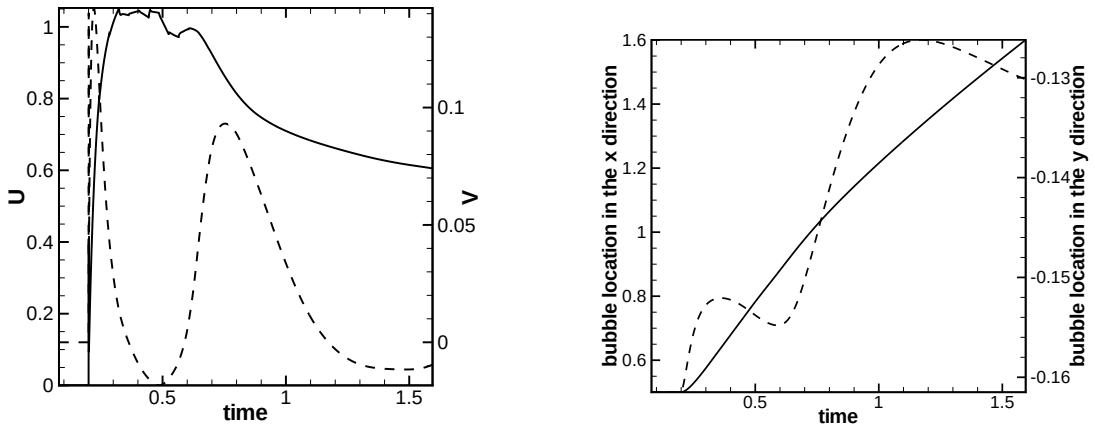

(a) Bubble velocity history

(b) Bubble location history

Figure 5.16: Velocity and location of the bubble history.— shows velocity and location in the x direction and $---$ shows velocity and location in the y direction. Time is expressed in $[ms]$, velocities are expressed in $[m/s]$ and bubble locations in $[mm]$.

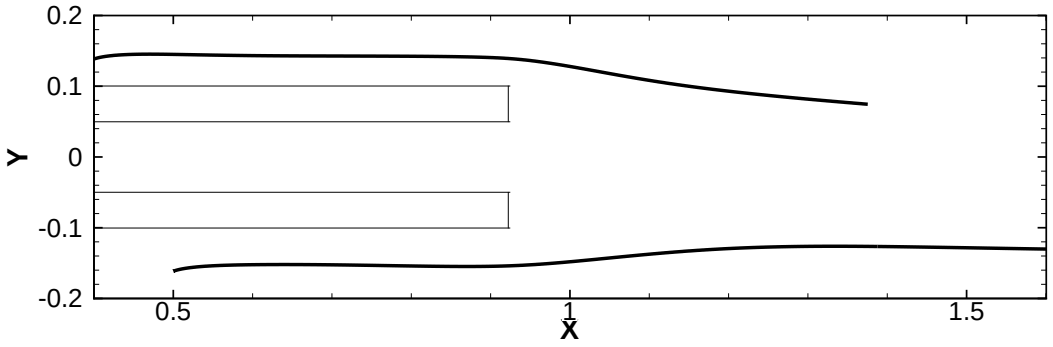

Figure 5.17: Bubbles trajectory in the geometry. Locations are expressed in $[mm]$.

domain, the interpretation of the commands is closely related to the evolution of the mass flow rate in the domain. Initially the mass flow rate drops in the top and bottom channels and increases in the center channel leads the controller to close the valve in the center channel (increase of the angle) and to fully open the top and bottom channels (decrease to 0 of the angle applied). As soon as the first bubble is released the mass flow rate increases suddenly in the bottom channel. In reaction, the controller shuts the bottom valve maintaining the top channel fully open in order to flush to remaining bubble. Once all the bubbles are released, the controller comes back to the nominal state where the flow is equalized in each channel.

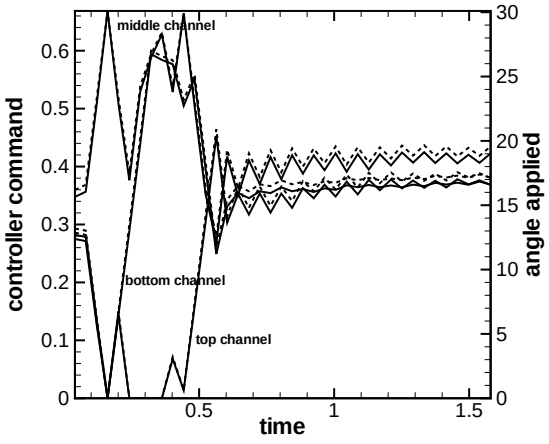

Figure 5.18: Controller output history correlated with angle applied to each valve.— shows the controller orders; − − − shows the angle applied to the valves. Time is expressed in $[ms]$, angles are expressed in degrees.

Chapter 6 – Conclusions and recommendations for future work

In this research a computational model has been used to compute flow through a 3 parallel microchannels domain. This model allowed to simulate flows with obstructions. In the case we looked at, one or two bubbles were injected inside the domain. The results show that the effect of such perturbations in an equalized flow are very strong. These perturbations of course can have dramatic consequences in terms of heat exchanger efficiency for example.

In order to provide a solution to help the flow to come back to an optimal regime, valves have been added at the entrance of each channel. From a computational point of view and contrary to the bubbles which are allowed to move freely in the domain. The valves are moved and operated by a controller. This controller designed by Chris Patton with the help of Dr. John Schmitt, decides of opening of each channel based on data of the mass flow rate in each channel. Pressure has been considered for a while unfortunately it wouldn't accurately predict what exactly happens in the channel. The best idea was then to consider the mass flow rate to achieve and compare it to the one captured by the sensors for each channel.

This approach gave extremely convincing results, after a long period of tests and calibration, a controller has been designed and is able to, first, equalize the mass flow rate in each channel very accurately, and second, react in case of sudden obstruction in one of the channels. If a drop in the mass flow rate is detected

the controller will force more and more flow through this channel which will have the result of increasing the hydrodynamic force acting on the bubble and then eventually flush it out of the domain.

Of course the exact behavior of the growing bubble couldn't be simulated. After a lot of attempts and different scenarii, it has been decided that the closest model to the physics considering what is possible to simulate, is to maintain the bubble along the wall computing the force acting on it at every time step. The bubble is artificially held fixed as long as the force is not sufficient to release it. Unfortunately no criterion could be found in order to compute the threshold to release the bubble. Our study showed that the possible range of force that can be applied on the bubble seems to be in the range of values observed from the literature in the cases of a bubble being attached to a wall in a microchannel.

This work shows excellent results in terms of efficiency to help to flush the bubble out of a microchannel. The action of the valves is significant and gives the ability to increase the force acting on the bubbles drastically. In case of a sudden nucleation of a bubble this method will massively reduce the time to resume an optimal flow, in certain cases or in certain conditions in which the surface tension would be too strong to allow the bubble to detach from the wall, this approach can allow to detach the bubble anyways.

Some of the limitations of the model are mentioned in this conclusion. The physical aspect of the phenomenon has been looked at and considered in order to try to make the simulation as realistic as possible. CFD limits what can be done but the overhaul simulation gives very good qualitative results and quantitative

results that are in the range of what has been observed.

However, several aspects could be slightly improved. The design of the valves motion could certainly be improved by allowing an actual rotation motion. This would allow smoother transition when the valves are rotating even if the controller updates are fairly small. The other improvement that can be made is about the controller. As mentioned before the controller reacts only to mass flow rate which might not be sufficient to detect a bubble. If the simulation works fine with only one bubble in the domain it causes troubles when two bubbles are injected. This is due to the fact that the controller doesn't actually detect a bubble it detects changes in the mass flow rate and try to correct it. That means that if we were to inject three bubbles, one in each channel, the controller would simply find a way to equalize the flow without trying to optimize the force applied on the bubbles. Addressing this issue would take to consider maybe other parameters. Pressure seems again to be the one to look at. But dealing with several parameters and different behaviors makes the design of the controller more challenging.

Future work would include simulations of applications where that kind of geometry can be used. One application for this geometry could be to use it for solar fuel, production of hydrogen by heating natural gas. This process involves flowing reactants through microchannels while they are heated by sun rays. The reaction rate depends on the respect of the optimum mass flow rate, but some secondary solid products might be formed which would lead in the situation studied here. Another extension of this work (already in progress) would be to study microchannel blocking due to bubbles aggregation and arching. This is computationally

challenging because in order to be relevant the simulation has to involve a large number of bubbles so that the probability of arching and blocking is sufficient.

Bibliography

[1] K.V. Sharp and R.J. Adrian. Shear-induced arching of particle-laden flows in microtubes. volume 51, page 61801.

[2] M. Martin, C. Patton, J. Schmitt, and S. V. Apte. Direct simulation based model-predictive control of flow maldistribution in parallel microchannels. *Journal of Fluids Engineering*, Under review, 2009.

[3] M. Martin, C. Patton, J. Schmitt, and S. V. Apte. Direct simulation based model-predictive control of flow maldistribution in parallel microchannels, under review. In *3rd International Conference on Micro- and Nanosystems (MNS), IDETC/CIE 2009.*

[4] W. Qu and I. Mudawar. Flow boiling heat transfer in two-phase micro-channel heat sinks—-i. experimental investigation and assessment of correlation methods. *International Journal of Heat and Mass Transfer*, 46(15):2755–2771, 2003.

[5] KA Triplett, SM Ghiaasiaan, SI Abdel-Khalik, and DL Sadowski. Gas–liquid two-phase flow in microchannels part i: two-phase flow patterns. *International Journal of Multiphase Flow*, 25(3):377–394, 1999.

[6] T. Cubaud. Transport of bubbles in square microchannels. *Physics of Fluids*, 16(12):4575, 2004.

[7] K.V. Sharp and R.J. Adrian. On flow-blocking particle structures in microtubes. *Microfluidics and Nanofluidics*, 1(4):376–380, 2005.

[8] W. Qu and I. Mudawar. Flow boiling heat transfer in two-phase micro-channel heat sinks—-ii. annular two-phase flow model. *International Journal of Heat and Mass Transfer*, 46(15):2773–2784, 2003.

[9] Carlos H. Hidroo David W. Fogg Jae-Mo Koo Juan G. Santiago Kenneth E. Goodson Thomas W. Kenny Evelyn N. Wang, Shankar Devasenathipathy. Liquid velocity field measurements in two-phase microchannel convection. In *3rd International symposium on Two-phase Flow Modeling and Experimentation*, September 2004.

[10] PC Lee, FG Tseng, and C. Pan. Bubble dynamics in microchannels. part i: single microchannel. *International Journal of Heat and Mass Transfer*, 47 (25):5575–5589, 2004.

[11] HY Li, FG Tseng, and C. Pan. Bubble dynamics in microchannels. part ii: two parallel microchannels. *International Journal of Heat and Mass Transfer*, 47(25):5591–5601, 2004.

[12] L.G. Bleris, J.G. Garcia, M.G. Arnold, and M.V. Kothare. Model predictive hydrodynamic regulation of microflows. *Journal of micromechanics and microengineering*, 16(9):1792, 2006.

[13] A. Mukherjee and S.G. Kandlikar. Numerical study of the effect of inlet constriction on bubble growth during flow boiling in microchannels. In *3rd International Conference on Microchannels and Minichannels, ICMM2005*, volume 75143, 2005.

[14] MA van der Hoef, M. van Sint Annaland, NG Deen, and JAM Kuipers. Numerical simulation of dense gas-solid fluidized beds: A multiscale modeling strategy. *Annual Review of Fluid Mechanics*, 40:47, 2008.

[15] S. V. Apte, M. Martin, and Patankar N. A. A numerical method for fully resolved simulation (frs) of rigid particle-flow interactions in complex flows. *Journal of Computational Physics, DOI: 10.1016/j.jcp.2008.11.034*, In Press, Corrected Proof, 2008.

[16] R. Glowinski, TW Pan, TI Hesla, DD Joseph, and J. Periaux. A fictitious domain approach to the direct numerical simulation of incompressible viscous flow past moving rigid bodies- application to particulate flow. *Journal of Computational Physics*, 169(2):363–426, 2001.

[17] NA Patankar. A formulation for fast computations of rigid particulate flows. *Center for Turbulence Research Annual Research Briefs 2001*, pages 185–196, 2001.

[18] NA Patankar, P. Singh, DD Joseph, R. Glowinski, and T.W. Pan. A new formulation of the distributed Lagrange multiplier/fictitious domain method for particulate flows. *International Journal of Multiphase Flow*, 26(9):1509–1524, 2000.

[19] R.D. Falgout and U.M. Yang. hypre: A Library of High Performance Preconditioners. In *Proceedings of the International Conference on Computational Science-Part III*, pages 632–641. Springer-Verlag London, UK, 2002.

[20] W. Qu, I. Mudawar, S.Y. Lee, and S.T. Wereley. Experimental and computational investigation of flow development and pressure drop in a rectangular micro-channel. *Journal of Electronic Packaging*, 128:1, 2006.

[21] R. Mittal, H. Dong, M. Bozkurttas, FM Najjar, A. Vargas, and A. von Loebbecke. A versatile sharp interface immersed boundary method for incompressible flows with complex boundaries. *Journal of Computational Physics*, 227(10):4825–4852, 2008.

[22] S. Marella, S. Krishnan, H. Liu, and HS Udaykumar. Sharp interface cartesian grid method i: An easily implemented technique for 3d moving boundary computations. *Journal of Computational Physics*, 210(1):1–31, 2005.

[23] R.D. Henderson. Details of the drag curve near the onset of vortex shedding. *Physics of Fluids*, 7:2102, 1995.

[24] C. Shu, N. Liu, and YT Chew. A novel immersed boundary velocity correction–lattice boltzmann method and its application to simulate flow past a circular cylinder. *Journal of Computational Physics*, 226(2):1607–1622, 2007.

[25] T. Ye, R. Mittal, HS Udaykumar, and W. Shyy. An accurate cartesian grid method for viscous incompressible flows with complex immersed boundaries. *Journal of Computational Physics*, 156(2):209–240, 1999.

[26] A.G. Kravchenko, P. Moin, and K. Shariff. B-spline method and zonal grids for simulations of complex turbulent flows. *Journal of Computational Physics*, 151(2):757–789, 1999.

[27] R. Mittal and S. Balachandar. Effect of three-dimensionality on the lift and drag of nominally two-dimensional cylinders. *Physics of Fluids*, 7:1841, 1995.

[28] D. Kim and H. Choi. Immersed boundary method for flow around an arbitrarily moving body. *Journal of Computational Physics*, 212(2):662–680, 2006.

[29] H. Dütsch, F. Durst, S. Becker, and H. Lienhart. Low-reynolds-number flow around an oscillating circular cylinder at low keulegan–carpenter numbers. *Journal of Fluid Mechanics*, 360:249–271, 1998.

[30] TA Johnson and VC Patel. Flow past a sphere up to a reynolds number of 300. *Journal of Fluid Mechanics*, 378:19–70, 1999.

[31] RH Magarvey and R.L. Bishop. Transition ranges for three-dimesnional wakes. *Canadian Journal of Physics*, 39(10):1418–1422, 1961.

[32] R. Clift, J.R. Grace, and M.E. Weber. *Bubbles, drops, and particles*. Academic Press, New York, 1978.

[33] R. Mittal. A fourier-chebyshev spectral collocation method for simulating flow past spheres and spheroids. *International Journal for Numerical Methods in Fluids*, 30(7):921–937, 1999.

[34] J. Kim, D. Kim, and H. Choi. An immersed-boundary finite-volume method for simulations of flow in complex geometries. *Journal of Computational Physics*, 171(1):132–150, 2001.

[35] S. Taneda. Experimental investigation of the wake behind a sphere at low Reynolds numbers. *J. Phys. Soc. Japan*, 11(10):1104–1108, 1956.

[36] MS Chong, AE Perry, and BJ Cantwell. A general classification of three-dimensional flow fields. *Topological Fluid Mechanics: Proceedings of the IUTAM Symposium, Cambridge, UK, 13-18 August 1989*, 1990.

[37] E. Anderson, Z. Bai, C. Bischof, S. Blackford, J. Demmel, J. Dongarra, J. Du Croz, A. Greenbaum, S. Hammarling, A. McKenney, and D. Sorensen. *LAPACK Users' Guide*. Society for Industrial and Applied Mathematics, Philadelphia, PA, third edition, 1999. ISBN 0-89871-447-8 (paperback).

[38] S. Lomholt, B. Stenum, and MR Maxey. Experimental verification of the force coupling method for particulate flows. *International Journal of Multiphase Flow*, 28(2):225–246, 2002.

[39] Y. Zhu. *Multivariable System Identification For Process Control*. Elsevier Science, 2001.

[40] R. Shridhar and D.J. Cooper. A Tuning Strategy for Unconstrained Multivariable Model Predictive Control. *Industrial and engineering chemistry research*, 37:4003–4016, 1998.